Gate-tunable Josephson diode

Mazur, G. P.; Van Loo, N.; Van Driel, D.; Wang, J.; Kouwenhoven, L. P.; Badawy, G.; Gazibegovic, S.; Bakkers, E. P.A.M.

DOI
10.1103/PhysRevApplied.22.054034

Publication date
2024

Document Version
Final published version

Published in
Physical Review Applied

Gate-tunable Josephson diode

G.P. Mazur[*,†]
QuTech and Kavli Institute of Nanoscience, Delft University of Technology, 2600 GA Delft, Netherlands and Department of Materials University of Oxford, Oxford, OX1 3PH, United Kingdom

N. van Loo,[†] D. van Driel, J.-Y. Wang, and L.P. Kouwenhoven
QuTech and Kavli Institute of Nanoscience, Delft University of Technology, 2600 GA Delft, Netherlands

G. Badawy, S. Gazibegovic, and E.P.A.M. Bakkers
Department of Applied Physics, Eindhoven University of Technology, 5600 MB Eindhoven, Netherlands

(Received 12 December 2022; revised 26 July 2024; accepted 10 October 2024; published 13 November 2024)

Superconducting diodes are recently-discovered quantum analogues of classical diodes. The superconducting diode effect relies on the breaking of both time-reversal and inversion symmetry. As a result, the critical current of a superconductor can become dependent on the direction of the applied current. The combination of these ingredients naturally occurs in proximitized semiconductors under a magnetic field, which is also predicted to give rise to exotic physics such as topological superconductivity. In this work, we use InSb nanowires proximitized by Al to investigate the superconducting diode effect. Through shadow-wall lithography, we create short Josephson junctions with gate control of both the proximitized weak link as well as the proximitized leads. When the magnetic field is applied perpendicular to the nanowire axis, the superconducting diode effect depends on the out-of-plane angle. In particular, it is strongest along a specific angle, which we interpret as the direction of the spin-orbit field in the proximitized leads. Moreover, the electrostatic gates can be used to drastically alter this effect and even completely suppress it. Finally, we also observe a significant gate-tunable diode effect when the magnetic field is applied parallel to the nanowire axis. Due to the considerable degree of control via electrostatic gating, the semiconductor-superconductor hybrid Josephson diode emerges as a promising element for innovative superconducting circuits and computation devices.

DOI: 10.1103/PhysRevApplied.22.054034

I. INTRODUCTION

Semiconducting diodes are rectifiers that allow current to flow in only one direction. As such, they are ubiquitously used in conventional electronics. Recently, superconducting analogues of diodes have been realized in V/Nb/Ta superlattices, where the critical current depends on the polarity of the applied current [1]. Consequently, it has been named the "superconducting diode effect" (SDE). The simultaneous breaking of both inversion symmetry and time-reversal symmetry has been identified as the critical ingredient for achieving the SDE [2,3]. Time-reversal symmetry is conventionally broken either through the application of a magnetic field or by use of magnetic materials [4]. Similarly, inversion symmetry is broken in systems with spin-orbit interaction (SOI), either through intrinsic structural asymmetry or via the application of electric fields. Interestingly, a correction to the critical current of superconducting films in the presence of an electric field was proposed in the context of superconductors with an intrinsic polar axis [2]. It has the form of $\alpha(\hat{\mathbf{c}} \times \mathbf{b}) \cdot \mathbf{J}$, where α is the Rashba spin-orbit constant, the unit vector $\hat{\mathbf{c}}$ points along the electric field, $\mathbf{b}$ is an external magnetic field, and $\mathbf{J}$ is the supercurrent density. Such a correction can be obtained purely from the Ginzburg-Landau theory when both inversion symmetry and time-reversal symmetry are broken. In recent years, however, there have been experimental reports suggesting that breaking of time-reversal symmetry is not necessarily needed for the diode effect. For example, nonreciprocal transport in noncentrosymmetric materials under time-reversal symmetry was recently predicted and experimentally observed [5–8].

To give more insight into the microscopic mechanism behind nonreciprocal critical currents, models that go beyond the Ginzburg-Landau theory have been proposed [9,10]. These models suggest that a finite Cooper-pair momentum is the underlying physical mechanism. In this picture, the energy of left-moving and right-moving carriers develops a finite Doppler shift plus or minus $\mathbf{q}\mathbf{v}_\mathbf{F}$ due to the finite momentum $\mathbf{q}$ acquired by the Cooper pairs [10]. On the other hand, theoretical studies on Josephson

[*]Contact author: greg.mazur@materials.ox.ac.uk
[†]These authors contributed equally to this work.

junctions (JJs) based on semiconducting nanowires predicted direction-dependent critical currents in the presence of SOI and breaking of time-reversal symmetry [11,12]. In this case, nonreciprocity of switching currents is caused by the interaction between multiple Andreev levels in the junction. In addition, the Meissner effect has been proposed [13] to give rise to a nonreciprocal critical current. Finally, a small out-of-plane magnetic field also leads to an SDE in type-II elemental superconductors [14].

Most of the work to date has observed the SDE in metallic systems or van der Waals materials with a high electron density [8], which implies that such devices cannot be tuned electrostatically. In this context, proximitized semiconductors are a convenient platform on which various parameters can be tuned with electrostatic gates. This includes the transparency [15] and the number of active modes in the junction, as well as the density in the proximitized region [16]. Note that in proximitized semiconductors, superconducting correlations are carried by electron-hole pairs, as opposed to a Cooper-pair condensate in regular metals. These pairs form Andreev bound states (ABSs) that can obtain a finite momentum due to the interplay between spin-orbit interaction and a Zeeman field [17–19]. The finite-momentum ABSs can be considered as the proximitized analogue of finite-momentum Cooper pairs. As a consequence, it is possible for an SDE to exist in a semiconductor in proximity to a regular superconductor, such as Al. Indeed, recent studies explored the SDE in weakly proximitized InAs [20], either in the form of Josephson junctions [21,22] or as a metallic wire defined on the InAs stack [23]. Planar Josephson junctions based on InSb nanoflags [24] and nanowires [25] are also reported to yield an SDE. Most studies have not reported a strong effect of electrostatic gating on the SDE [21–24]. Therefore, superconducting diodes would have limited use as circuit elements of superconducting computation devices or quantum computers. Instead, a greater degree of control is desired [26,27], similarly to the electrical tunability of state-of-the-art quantum electronics based on semiconductors [28].

In this article, we demonstrate the presence and control of the SDE in semiconductor-superconductor hybrid Josephson junctions by means of electrostatic gating. Separate gate control of the electron density underneath the proximitized leads as well as in the proximitized weak link enables us to isolate their contribution to the observed SDE. Furthermore, we show that the efficiency of the SDE scales with the switching current in the JJ. In addition, we demonstrate that the SDE can also occur when a magnetic field is applied parallel to the nanowire axis and hence parallel to the current flow. Dual gating of the proximitized weak link and the proximitized leads allows the InSb/Al JJ to act as a Josephson field-effect transistor as well as a superconducting diode. As such, it emerges as a promising platform for the development of superconducting circuits.

II. EXPERIMENTAL SETUP

We study a Josephson junction made from an InSb nanowire coupled to an Al shell, which has critical temperature $T_C \approx 1.8$ K [15]. Figure 1(a) shows a schematic of such a device together with the measurement circuit. The InSb nanowire has a diameter of 110 nm and is placed on a HfO_2 dielectric, which separates the device from a set of local bottom gates. The device features two distinct gates: A voltage on the tunnel gate V_{TG} is used to control the proximitized weak link, where it affects both the number of active modes and their transparency. On the other hand, a voltage on the super gates V_{SG} controls the electron density in the proximitized leads (i.e., the InSb segments underneath the Al). In recent work [16] we showed that this gate can also be used to adjust the semiconductor-superconductor coupling, resulting in gate-tunable properties such as the induced gap and g-factor. A current bias I is applied through the junction, and the resulting voltage drop V is measured. The sample is fabricated by means of our shadow-wall-lithography technique [15,29]. This fabrication method allows us to create proximitized weak links as short as 50 nm [30] such that the device is expected to be in the short-junction limit. Since the length of the proximitized weak link is shorter than the coherence length, transport is dominated by tunnel processes via Andreev bound states. In short junctions, transport is also sensitive to properties of the proximitized leads [31,32]. Figure 1(b) illustrates the cross section of the hybrid together with the coordinate system used throughout this work.

To investigate the SDE, we apply a current bias to the sample and look for a difference in the detected critical current between the forward-bias and reverse-bias measurements. In Fig. 1(c), we show an example I-V curve under conditions where an SDE should be observed (i.e., a finite magnetic field perpendicular to the nanowire axis). As I is swept from negative to positive (blue curve), the measured voltage first drops to zero at the retrapping current I_{rt}^{+}. At the positive switching event I^{+}, the measured voltage jumps again to a finite value. Similarly, the negative retrapping and switching events I_{rt}^{-} and I^{-} can be obtained by reversal of the current bias polarity (red curve). In this case, a small difference between $I^{+} = 18.4$ nA and $|I^{-}| = 17.7$ nA is observed, evidencing the SDE. As the switching current in Josephson junctions is stochastic [33,34], we use a fast-switching detection method [23,35] to accurately resolve its value (see Appendix A 3). An example of a switching-current distribution obtained with this method is shown in Fig. 1(d), where histograms for 200 switching events (I^{+}, I^{-}) are plotted. From these distributions, the average switching currents for the forward bias I_{sw}^{+} and the reverse bias $|I_{sw}^{-}|$ are estimated. These values of the switching current are then used to calculate the SDE efficiency $\eta = (I_{sw}^{+} - |I_{sw}^{-}|)/(I_{sw}^{+} + |I_{sw}^{-}|)$.

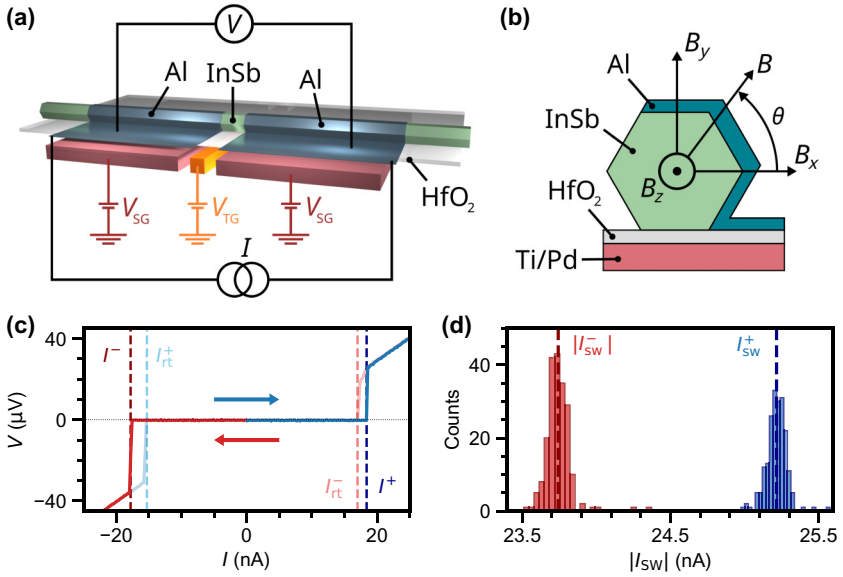

FIG. 1. Device and measurement technique. (a) Measurement circuit, depicting a Josephson junction in the current-bias configuration. The InSb nanowire (green) is covered by an Al shell (blue), which forms a connection to the film on the substrate. The electronic density underneath the shell is controlled via the super gates (red), and the junction transparency is tuned with the tunnel gate (orange). (b) Hybrid cross section. The magnetic field angle θ is defined as the angle in the plane perpendicular to the nanowire axis, starting at $\theta = 0^\circ$ when the applied magnetic field is along B_x. (c) Example of I-V curves showing nonreciprocal behavior. Blue and red curves display forward and reverse current bias, respectively. Positive and negative switching current (I^+, I^-) and retrapping current (I^+_{rt}, I^-_{rt}) are marked with dashed lines. (d) Example of switching-current histograms, each consisting of switching events (I^+, I^-) from 200 I-V curves. The average value of the distributions is labeled "$|I^-_{\mathrm{sw}}|$" and "I^+_{sw}" for the negative and positive switching currents, respectively.

III. RESULTS

We start the investigation of the SDE in our system by rotating the magnetic field ($B = 12$ mT) in the plane perpendicular to the nanowire axis, so that the direction of the current remains perpendicular to the applied field. We set the tunnel gate voltage to a high $V_{\mathrm{TG}} = 3.61$ V. At this voltage, the normal-state conductance of the junction is on the order of three to five conductance quanta (see Fig. 19). In the limit of a short Josephson junction, where each transverse subband gives rise to a single mode, we estimate there are around six to ten active modes. Consequentially, this maximizes the switching current in the proximitized weak link. The dependence of the diode efficiency on the magnetic field angle and super-gate voltage is shown in Fig. 2(a). In the top panel, we identify two distinct behaviors of the SDE. For $V_{\mathrm{SG}} > 1.15$ V, we observe a finite diode efficiency that exhibits a sinusoidal dependence on the angle of the magnetic field. A line cut in this regime taken at $V_{\mathrm{SG}} = 1.61$ V is shown in the bottom panel of Fig. 2(b). A sinusoidal fit of $\eta(\theta)$ allows us to extract the angle with maximum efficiency θ_{max} as well as the efficiency η_{max} at that angle (see additional data in Appendix B). From the fit for this particular line cut, we estimate $\theta_{\mathrm{max}} = 105^\circ$ and $\eta_{\mathrm{max}} = 0.08$. In contrast, the SDE is diminished and the field-angle dependence is almost absent at $V_{\mathrm{SG}} < 1.15$ V. This is emphasized in the top panel of Fig. 2(b), which shows a line cut taken at $V_{\mathrm{SG}} = 0.72$ V. We execute the fitting procedure for all values of V_{SG} to determine θ_{max} and η_{max} as we vary the gate voltage. The results are presented in the middle and bottom panels of Fig. 2(a), respectively. We see that the estimated θ_{max} remains roughly constant at $V_{\mathrm{SG}} > 1.15$ V at $\theta_{\mathrm{max}} \approx 105^\circ$. We interpret this angle to be the direction of the spin-orbit field in the proximitized leads $\theta_{\mathrm{max}} = \theta_{\mathrm{SO}}$, which we elaborate on in Sec. IV. In contrast, η_{max} is modulated between approximately 1% and approximately 8% and does not simply increase with V_{SG}. In both panels, the gray data points correspond to a poor sinusoidal fit of $\eta(\theta)$ with an R^2 value of 0.85 or less. See Fig. 10 in Appendix B for the underlying switching-current maps and the estimation of the fitting error. As V_{SG} also modulates the magnitude of the switching current, we plot the maximum diode efficiency versus the average switching current in Fig. 2(c). Interestingly, an increase in η_{max} appears to correlate with higher switching currents. This observation naturally raises the question of whether the observed SDE can be attributed to the contribution from the proximitized leads of the device or to the increasing transparency of the junction due to capacitive coupling between the gates.

To answer this question, we note that the transparency of the junction, as well as the number of modes in the junction, can be adjusted directly through the use of the

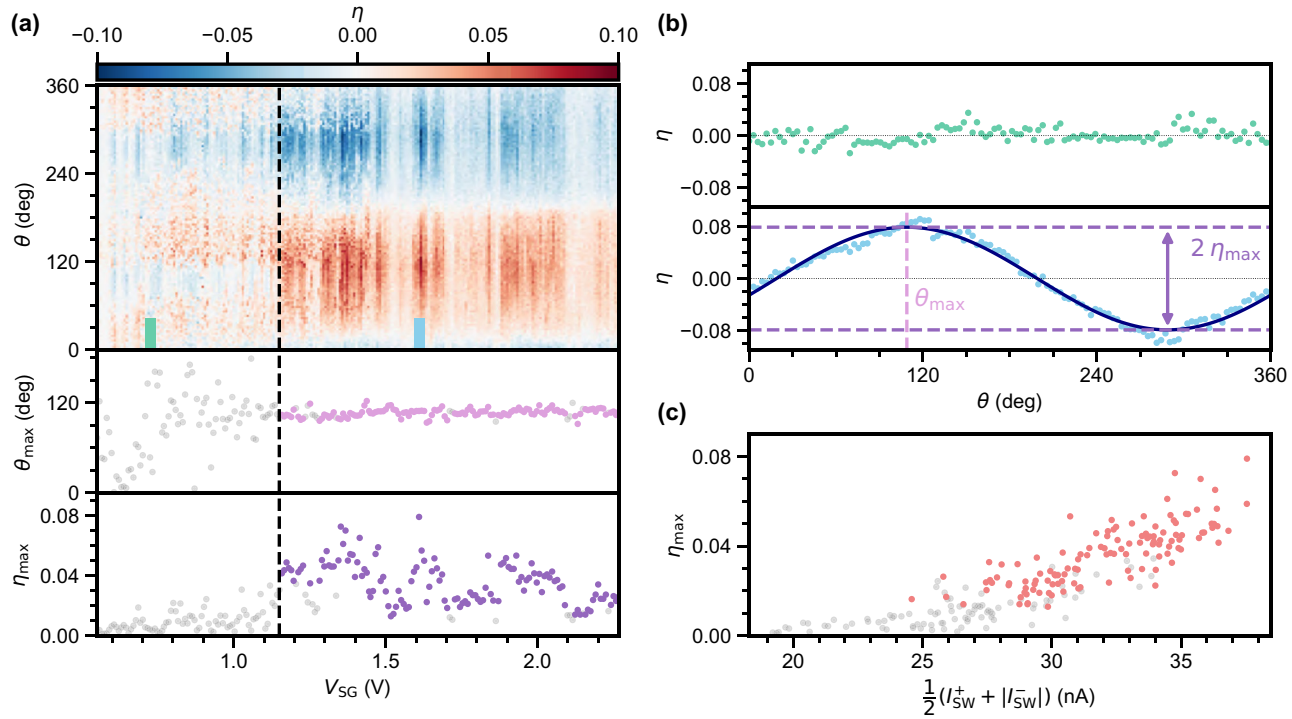

FIG. 2. Dependence of superconducting diode effect on super-gate voltage. (a) Top: η as a function of super-gate voltage V_{SG} and θ, taken with $V_{TG} = 3.61$ V and $B = 12$ mT. Middle: Estimation of θ_{max}. Bottom: η_{max} as a function of V_{SG}. The dashed black line indicates that the diode effect is suppressed at $V_{SG} < 1.15$ V. (b) Top: Lack of an SDE at $V_{SG} < 1.15$ V. Bottom: Presence of an SDE at $V_{SG} > 1.15$ V. Line cuts taken from the top panel in (a) at locations indicated by the colored bars. In the bottom panel, the dashed pink line specifies θ_{max}, whereas η_{max} is depicted by the dashed purple lines. (c) η_{max} as a function of average switching current, taken along $\theta = 105°$. In all panels, gray data points correspond to a poor sinusoidal fit ($R^2 < 0.85$) of η as a function of θ.

tunnel gate. We proceed by fixing the super-gate voltage V_{SG} to 2 V, above the previously identified threshold of 1.15 V.

Next, the tunnel gate voltage V_{TG} is varied such that switching current $|I_{sw}|$ is modulated from 5 to 25 nA. We again vary the angle θ of the perpendicular magnetic field with an amplitude of 12 mT, while measuring the diode efficiency. The results of this experiment are presented in Figs. 3(a)–3(c), where in Fig. 3(a) we show the evolution of the SDE. The effect is present for almost all gate values, while η is modulated with V_{TG}. Interestingly, the extracted θ_{max} remains constant as a function of the junction transparency at $\theta_{max} = 105°$. In particular, η remains sinusoidal in θ [see, for example, Fig. 3(b)], and adjustments of V_{TG} affect only the amplitude. The scaling of η_{max} with I_{sw} is no longer monotonic, while the highest efficiency is still observed for high switching currents $|I_{sw}|$ in the range 15–20 nA [Fig. 3(c)]. Moreover, we are able to measure an appreciable SDE even at very low switching currents $|I_{sw}|$ on the order of 5 nA. This confirms that the observed crossover in Fig. 2 cannot be attributed to a reduced switching current as a result of, for example, capacitive coupling between the tunnel gate and the super gate. On the other hand we note that for switching currents as small as approximately 1 nA, the SDE ($V_{TG} = 2.15$ V) is not detectable within our experimental resolution. The situation is drastically different for $V_{SG} = 0.8$ V, which we present in Figs. 3(d)–3(e). Here, we adjust the tunnel-gate-voltage range such that it covers a similar range of switching currents $|I_{sw}|$, 5 and 25 nA. In Fig. 3(d), we see that the efficiency of the SDE is generally lower. It is often nonsinusoidal in θ, and θ_{max} varies strongly with V_{TG}. An example is shown in Fig. 3(e), where the angle with the maximum SDE is close to 0°. The observed η_{max} is mainly below 1%, even for the highest switching currents shown in Fig. 3(f).

Next we turn our attention to the dependence of the SDE on the magnitude of the magnetic field. The results are shown in Fig. 4(a), where the polar axis is the field angle θ and the radial axis represents the field magnitude B. Line cuts at various angles are shown in Figs. 4(b)–4(d). In most the experiments to date, the efficiency of the diode does not simply increase linearly with the magnetic field. Instead, the linear dependence holds only for low values of B, after which it peaks at a particular field value before it decays to zero, as can be seen in Fig. 4(d), where the field is applied along previously identified $\theta_{max} = 105°$. In our device, we also find an unexpected deviation from that behavior when the magnetic field is applied along $\theta = 67°$ [see Fig. 4(c)]. Here, η increases linearly before

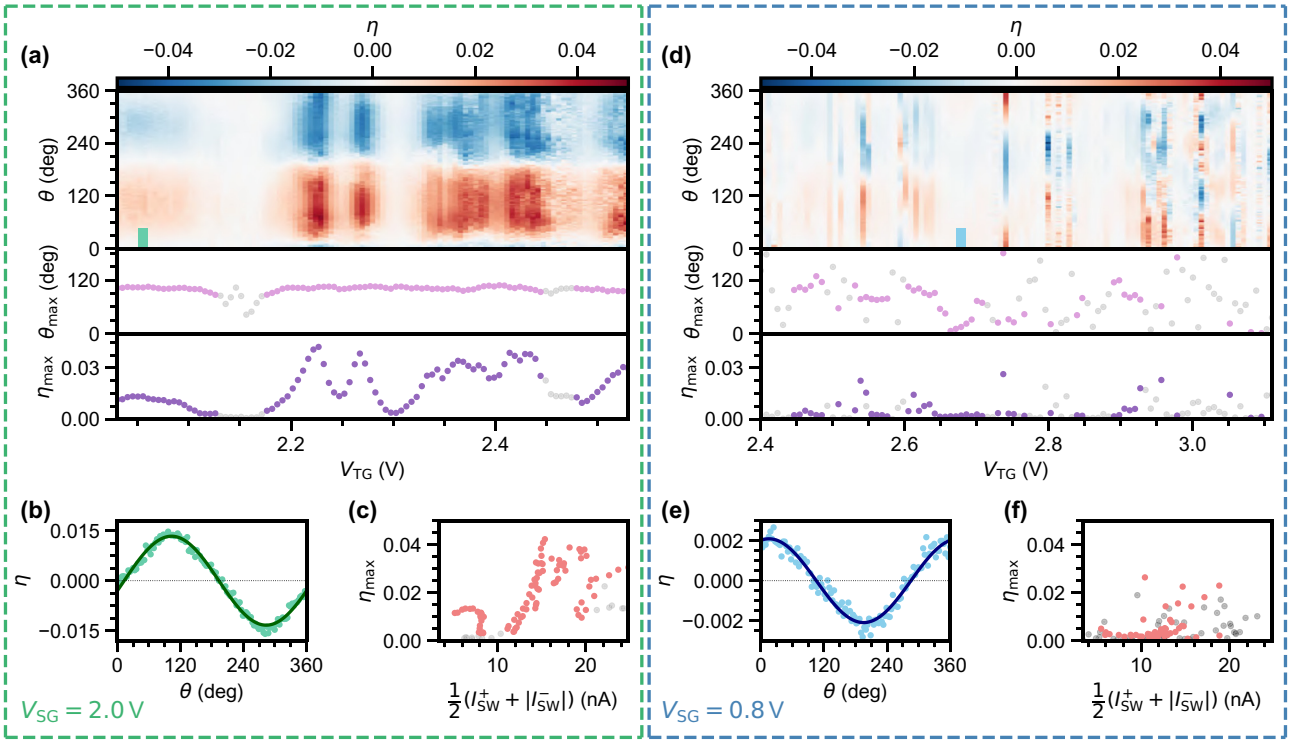

FIG. 3. Dependence of superconducting diode effect on tunnel-gate voltage. (a)–(c) Dependence on V_{TG} at a high super-gate voltage $V_{SG} = 2.0$ V. (a) Top: η as a function of V_{TG} and θ. Middle: Estimation of θ_{max}. Bottom: η_{max} as a function of V_{TG}. (b) Example of η taken at the location indicated by the colored bar in (a). (c) η_{max} as a function of average switching current, taken along $\theta = 105°$. (d)–(f) Dependence on V_{TG} at a low super-gate voltage $V_{SG} = 0.8$ V. (d) Top: η as a function of V_{TG} and θ. Middle: Estimation of θ_{max}. Bottom: η_{max} as a function of V_{TG}. (e) Example of η taken at the location indicated by the colored bar in (d). (f) η_{max} as a function of average switching current, taken along $\theta = 105°$. In all panels, gray data points correspond to a poor sinusoidal fit ($R^2 < 0.85$) of η as a function of θ. Data taken at $B = 12$ mT.

saturating at $B = 10$ mT (see Fig. 17 for an extended magnetic field range). In addition, we note that the SDE is negligible whenever the magnetic field is applied perpendicular to θ_{max} at $\theta = 15°$, as shown in Fig. 4(b).

Lastly, we examine the impact of a parallel magnetic field on the SDE in our system. The results of this experiment are presented in Fig. 5. At zero magnetic field [top panel in Fig. 5(b)], the SDE is predominantly absent, with occasional spikes at conductance resonances. When B_z is increased, the SDE becomes more pronounced and η exhibits multiple changes of sign as a function of V_{SG}, as shown in the bottom panel of Fig. 5(b). Strikingly, our experimental data can once again be split into two different characteristic regimes. For the low super-gate region below 1.15 V, the SDE exhibits frequent polarity flips as well as high efficiency. At voltages above that threshold, the SDE is still present, but, in general, with lower intensity and with fewer polarity switches. This is best seen by comparison of the top and bottom panels of Fig. 5(c). The top panel shows a line cut at $V_{SG} = 1.1$ V, which exhibits a large η as well as a polarity switch. The bottom panel, on the other hand, presents a line cut along $V_{SG} = 1.3$ V, where the SDE is strongly quenched.

IV. DISCUSSION

One of the primary findings of our experimental work is a sinusoidal angle dependence of the SDE over a large range of positive values of V_{SG}. Such a dependence can be interpreted by taking into account the role of spin-orbit interaction proposed in Edelstein's model for polar superconductors [2], which predicts a correction to the critical current in the form of $\alpha(\hat{\mathbf{c}} \times \mathbf{b}) \cdot \mathbf{J}$. From this prediction, we expect a diode efficiency $\eta \propto \cos(\theta)$, which is maximum whenever the magnetic field aligns with the direction of the spin-orbit field. The spin-orbit interaction in our devices originates from the electric field applied on the super gates. As the Al film covers three facets of the hexagonal nanowire and extends onto the substrate [Fig. 1(b)], the electric field lines bend towards the metallic half-shell [36]. This agrees well with the observed maximum-efficiency angle $\theta_{max} = 105°$. On a second device (device B, Fig. 23), the extracted θ_{max} is similar at $\theta_{max} = 110°$. This is also in agreement with the results obtained in a work that studied the dependence of spin-orbit interaction on the induced superconducting gap [36] for devices in the same geometry.

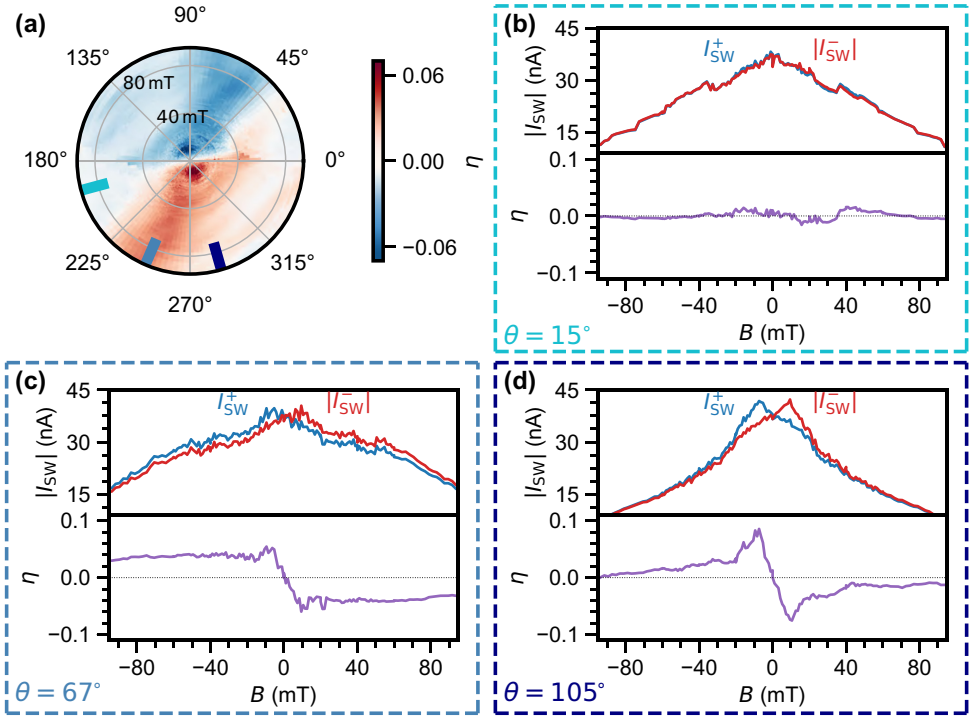

FIG. 4. Evolution of the superconducting diode effect as a function of magnetic field perpendicular to the nanowire axis. (a) Polar plot of η as a function of θ (polar axis) and field magnitude B (radial axis), taken at $V_{SG} = 2.21$ V and $V_{TG} = 3.60$ V. (b)–(d) I_{sw}^{+}, $|I_{sw}^{-}|$, and η as a function of B taken at various angles. Perpendicular to the maximum-efficiency angle [$\theta = 15°$, (b)], no SDE is observed. At $\theta = 67°$ [(c)], the SDE persists in a high magnetic field. At the maximum-efficiency angle [$\theta = 105°$, (d)], the SDE increases linearly at $B = 0$ T and reaches a maximum at $B = 10$ mT.

A related observation is the dependence of the SDE on the super-gate voltage V_{SG}. As depicted in Fig. 2(a), we notice a sharp onset in the SDE efficiency η and the sinusoidal angular dependence. There is a striking similarity between this sharp onset of the SDE and the tunable semiconductor-superconductor coupling observed for InSb/Al hybrids [16]. The tunable coupling is reflected in a strong gate tunability of the size of the induced gap as

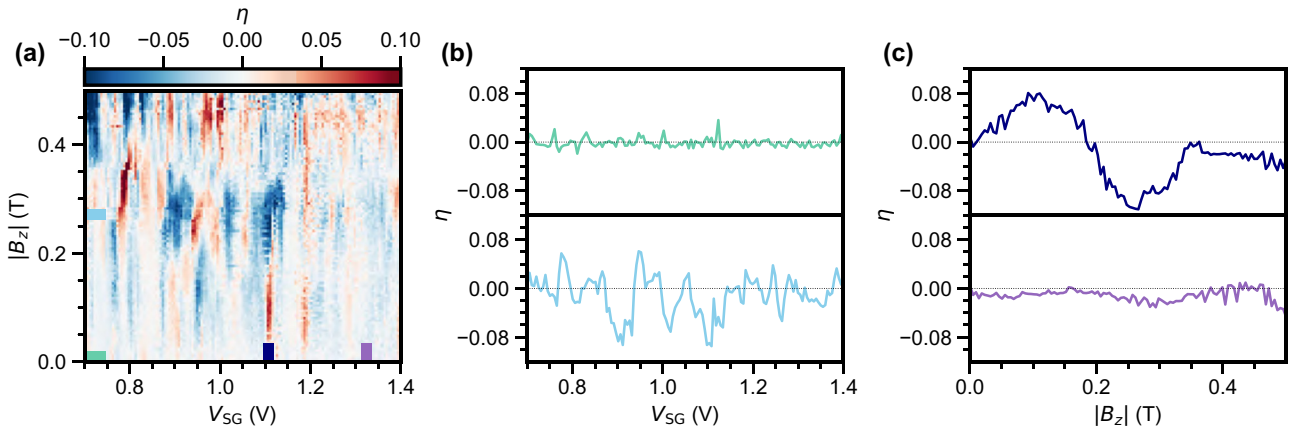

FIG. 5. Evolution of the superconducting diode effect as a function of magnetic field parallel to the nanowire axis. (a) η as a function of V_{SG} and B_z. (b) Examples of η as a function of V_{SG} taken at locations indicated by the colored bars in (a). At finite field (bottom), the SDE frequently changes sign and the efficiency is strongly modulated by the tunnel-gate voltage. (c) Examples of η as a function of B_z taken at locations indicated by the colored bars in (a). Depending on V_{SG}, the magnetic field can both increase the diode efficiency and cause a sign inversion. Data taken at $V_{TG} = 3.615$ V.

well as the g-factor. As the SOI is modulated by the coupling as well [37,38], this provides an explanation for the difference between the low and high super-gate regimes. We interpret our observations as follows. For high V_{SG}, the system can be seen as S-S'-N-S'-S, where S is the Al shell, S' is the proximitized semiconductor, and N is the proximitized weak link. In this regime, the hybrid inherits semiconducting properties such as a high g-factor and appreciable SOI. The presence of a finite SOI in addition to a Zeeman field results in a finite momentum of the ABSs that form in the proximitized leads [17–19]. In contrast, for low V_{SG}, the hybrid should be seen as S-N-S, where S represents the metallic (Al-like) leads with weak SOI. In the absence of SOI, the ABSs in the leads do not obtain a finite momentum, resulting in the suppression of the SDE (For completeness, we present dependence of η on V_{SG} at 60 mT in the Fig. 18). Still, the proximitized weak link itself also possesses a strong SOI, which can lead to a finite SDE. In particular, changing the tunnel-gate voltage modifies the confinement in the junction. The conductance resonances originating from this confinement [39] yield a fluctuating spin-orbit direction [40]. This explains the existence of an erratic SDE in the low V_{SG} regime as originating from SOI in the proximitized weak link.

It is worth mentioning that recently it was shown that the SDE can also arise in systems without SOI [13]. In this framework, screening currents present in the superconducting shell due to the Meissner effect lead to a spatially varying order parameter. This can equally well result in the formation of finite-momentum ABSs in proximitized material. In the case of our study, however, the magnetic field has a maximum contribution to orbital effects in the Al shell when the field is oriented perpendicular to the middle facet of the nanowire, at $\theta = 30^\circ$ [see Fig. 1(b)]. However, we observe a maximum value of η for magnetic field angle $\theta_{max} = 105^\circ$, almost perpendicular to this direction (see Fig. 12 for corresponding switching current maps). Moreover, η measured along $\theta = 15^\circ$ is close to zero in a magnetic field range from 100 to -100 mT. Related to those observations, the Meissner effect in the Al shell does not seem to be the dominant mechanism explaining our results. Orbital effects might also have a direct effect on ABSs formed in the semiconductor; however, it is presently unclear how this might influence the SDE.

The SDE dependence on the magnetic field magnitude (as shown in Fig. 4) also points towards the presence of finite-momentum ABSs. In particular, the dependence of η on θ evolves from being proportional to $\sin(\theta)$ to being proportional to $\sin(\pi \sin(\theta))$ as the magnetic field amplitude is increased (see also Fig. 13 in Appendix B). The angular dependence of the diode efficiency measured as a function of the magnitude of the magnetic field looks nearly identical to the results reported for $NiTe_2$ [19]. There, this behavior was directly attributed to the presence of finite-momentum Cooper pairing. This observation suggests that the phenomenological theory of finite-momentum Cooper pairing can be universally applied to different material systems and may help to discriminate between various physical origins of the observed SDE. Proximitized InSb is particularly appealing in this context, as it has a fairly simple Fermi surface [41] and the proximity effect has been widely studied in this material [16,42], which should lead to a simplification of theoretical studies.

Most of the models to date require the applied magnetic field to be parallel to the spin-orbit axis and perpendicular to the current flow [2,10], with finite-momentum Cooper pairing as the microscopic origin. However, there are also several predictions regarding an SDE with the magnetic field applied parallel to the current flow. We discuss the applicability of those models to the experimental results presented in Fig. 5 (see Fig. 14 for switching current maps). Short nanowire Josephson junctions with SOI in the presence of a Zeeman field were theoretically studied by Yokoyama *et al.* [11,12]. When multiple conduction channels are formed within the proximitized weak link, the Andreev levels interact and hybridize with each other due to interplay between disorder and SOI. On the application of an external magnetic field, they also become subject to a Zeeman splitting. As a result, time-reversal symmetry is broken and the energy of these levels is no longer equal with respect to sign inversion of the phase $E_N(-\varphi) \neq E_N(\varphi)$, where E_N is the energy of the Andreev levels and φ is a phase difference across the junction. This inequality also leads to an SDE. Similarly, a recent model [9] predicted that in the presence of a finite out-of-plane component, an in-plane Zeeman field is expected to drive subband transitions that should manifest themselves as an increase of the SDE efficiency as well as inversion of the polarity. It is of particular interest for the study of topological superconductivity, as this information could be used to identify regions in parameter space where topological superconductivity is predicted to emerge.

We suspect that the SDE in a parallel magnetic field (as shown in Fig. 5) originates primarily from interaction between ABSs in the proximitized weak link. To understand this, we notice that under that particular gate configuration, the normal-state conductance is similar to that in Fig. 2 and the number of modes can be estimated as 6–10. We also note that the data can once again be divided into two sections. In contrast to the case of a perpendicular magnetic field, the SDE efficiency is greatest at low V_{SG}, while it remains strongly modulated with V_{TG} (see Fig. 22). In this regime, the electron density in the hybrid segments of the nanowire is expected to be low [16,43,44]. Conversely, we keep $V_{TG} = 3.615$ V, which ensures a high density in the InSb weak link. The corresponding potential profile (e.g., a low V_{SG} in combination with a high V_{TG}) results in additional confinement for the Andreev levels formed in the proximitized weak link. A change in the

confinement has been shown to change the magnitude and direction of the SOI [40], and also affects the scattering between different levels. Together, the interplay between these effects can modify the Andreev level spectrum in the weak link and, as a consequence, also affect the SDE. In particular, a phase shift $\varphi \approx \pi$ in the current-phase relation of the Andreev levels can generate a switch in the polarity of the SDE, as predicted by Yokoyama *et al.* [12]. Such a phase shift can originate from either the changing confinement or Zeeman splitting of the Andreev levels in a magnetic field. On the other hand, Legg *et al.* [9] also predicted sign changes in the SDE polarity as the result of subband crossings in the hybrid. However, in this proposal, a magnetic field component perpendicular to the nanowire axis is also required, which we do not apply in the current experiment. Furthermore, the addition of a small out-of-plane component does not significantly alter the picture (see additional data in Fig. 24). Thus, we cannot attribute our observations to subband physics.

V. CONCLUSIONS

In conclusion, we have demonstrated the existence and gate tunability of the Josephson diode effect in proximitized InSb nanowires. We have identified that it has a strong dependence on the electronic density both in the leads and in the proximitized weak link. For a high density in the leads, the angle for which diode efficiency is maximized is fixed. We interpret this angle as the direction of the spin-orbit field in the proximitized leads, which is in agreement with previous work on devices with a similar geometry [36]. Likewise, the proximitized weak link can give rise to the SDE, albeit with much lower efficiency. There, the maximum angle is strongly modulated by the tunnel-gate voltage, which we assign to a modification of the confinement potential. Our measurements at high magnetic fields point to finite-momentum Andreev bound states as a microscopic mechanism for the observed diode effect, in accordance with recent theoretical proposals and experiments [13,19]. Finally, we show that the superconducting diode effect is also present when the field is applied parallel to the nanowire axis.

This work demonstrates the impact of the electronic density in the leads and the proximitized weak link on the SDE. As a consequence, gate-tunable superconducting diodes can be used as a building block of superconducting quantum devices. For example, proposals already exist that envision the use of these devices as on-chip gyrators and circulators [26]. Moreover, the gate-tunable switching current allows the InSb/Al JJ to act as a Josephson field-effect transistor—establishing it as a highly versatile and promising circuit element for superconducting electronics. In addition, this system can be readily used to create superconducting quantum interference devices, in order to investigate the current-phase relation of a Josephson diode. In this case, one arm of the loop is tuned to the regime with a strong SDE and well-defined maximum SDE angle, while the reference arm can be tuned to a trivial regime without any SDE. As theoretically proposed, gate-tunable junctions can also be embedded in many-loop interferometers to achieve unprecedentedly high efficiencies [45]. Further improvements to the circuits can be made through embedding quantum dots in the junction, which may allow the achievement of the SDE at zero magnetic field [46].

Raw data presented in this work and the data-processing and data-plotting codes are available at [47].

ACKNOWLEDGMENTS

We thank Raymond Schouten for the technical support with switching-current measurements. We thank Liang Fu, Chun-Xiao Liu, and Mert Bozkurt for helpful discussions. This work was financially supported by the Dutch Organization for Scientific Research (NWO) and Microsoft Corporation Station Q.

G.P.M. and N.v.L. conceived the experiment. G.P.M. and N.v.L. fabricated and measured the devices. J.Y.W. and D.v.D. assisted with sample fabrication and/or measurements. G.P.M. and N.v.L. analyzed the transport data. G.B. S.G., and E.P.A.M.B synthesized the nanowires. G.P.M. and N.v.L. wrote the manuscript with valuable input from all authors. L.P.K. supervised the project.

APPENDIX A: METHODS

1. Device fabrication

The InSb/Al hybrids presented in this work are fabricated on prepatterned substrates, following the shadow-wall-lithography technique described in Refs. [15,29]. Specific details of the substrate fabrication, nanowire oxide removal, and superconductor deposition can be found in the supplementary information in Refs. [16,48].

2. Setup for measurements

Samples are measured in a dilution refrigerator with a base temperature of approximately 20 mK, equipped with a three-axis vector magnet. We note that the switching current measured in a Josephson junction has a stochastic nature. As we are looking for quite-small switching currents, a single I-V curve is not enough to systematically investigate the superconducting diode effect. We present the I-V curved obtained through standard. Instead, we use a setup that allows us to record a large number of switching events and look for the average of the distributions obtained. The circuit used for this is shown in Fig. 6(a), and a false-color scanning electron micrograph is shown in Fig. 6(b). We apply a current bias I with a triangular waveform and a frequency of 20 Hz. In Fig. 6(c), we show a

cartoon of a single period of this wave in the bottom panel, and the resulting voltage drop on the sample in the top panel. During the first half-period of the wave, the current is swept from negative to positive bias. The junction goes from a resistive state into the superconducting state, where the voltage drop $V = 0$ μV. As the bias is increased, the junction switches again to the normal state, which causes the voltage to jump to a finite value. Throughout the measurement, we use a threshold voltage $V_{\rm th}^{+}$ (light-blue line). The circuit detects the voltage drop on the sample surpassing the threshold voltage, and sends an optical trigger to the current meter at that time t^{+} (dotted dark-blue line). The current meter records the current bias value I^{+} (dashed dark-blue line). In the second half of the wave's period, the situation is reversed. The bias now sweeps from positive to negative, and at some point the junction switches from the superconducting state to the normal state. At this time t^{-} the voltage drop on the sample drops below the negative threshold $V_{\rm th}^{-}$, and the current meter records the current bias I^{-}. For each data point ($V_{\rm SG}$, $V_{\rm TG}$, B, θ, B_z) presented in this work, 200 periods of the waveform are swept, resulting in 200 recorded values of I^{+} and I^{-} each. In Fig. 7, four examples of resulting switching-current distributions are shown for various values of the magnetic field. The reported switching currents $I_{\rm sw}^{+}$ and $|I_{\rm sw}^{-}|$ in this work are calculated as the mean of each 200-data-point distribution. At low values of B, the switching-current distributions are typically broader as evidenced by their standard deviation σ [Fig. 7(a), bottom panel]. We suspect this is the result of heating of the mixing chamber due to the presence of magnetic components in the sample puck. For completeness we are presenting the data obtained via standard 4-probe I-V measurement in the Fig. 8.

We used Delft University of Technology homemade electronics tailor-made for the cryogenic measurements. A description of the module performing optical detection is described in Ref. [49]. We used a Keithley 2000 multimeter to read the output of the module and a Keysight 33509B arbitrary-waveform generator to generate a triangular wave.

3. Data analysis

Whenever the magnetic field is applied in the plane perpendicular to the nanowire axis, the diode efficiency is modulated. The angle with maximum SDE efficiency can be determined by one fitting the diode efficiency $\eta(\theta)$:

$$\eta(\theta) = a\sin(\theta + c) + d, \qquad \theta_{\rm max} = -c + 90^{\circ}, \tag{A1}$$

where the amplitude a, phase c, and offset d are free fitting parameters, while the period of the sine is fixed to 360°. The fitting procedure is applied to various 2D maps

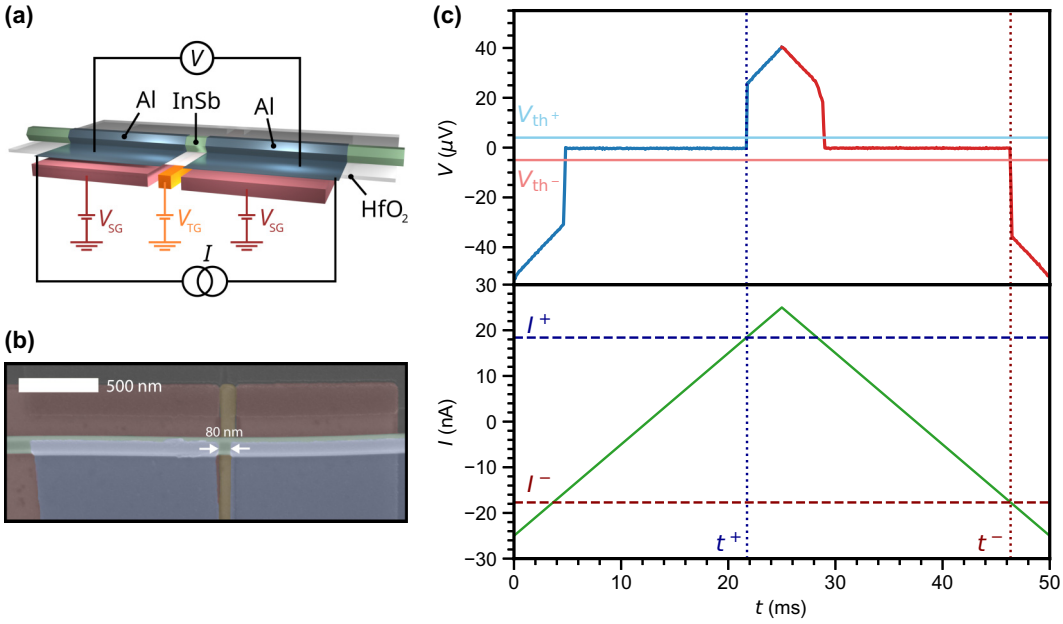

FIG. 6. Measurement circuit and technique. (a) Electrical circuit used to measure switching-current distributions. (b) False-color scanning electron micrograph of a Josephson junction that is lithographically identical to the measured devices. The junction is on the order of approximately 80 nm long, and the hybrid segments are on the order of approximately 1 μm long. (c) Acquirement of a single switching-current event. Top: Resulting voltage drop V on the junction. Bottom: Applied triangular wave with a frequency of 20 Hz. On the up sweep, the circuits detects the surpassing of the threshold voltage $V_{\rm th}^{+}$ by the sample voltage. This sends an optical trigger to the current meter, which records the switching-current event I^{+}. Similarly, I^{-} is recorded on the down sweep of the wave.

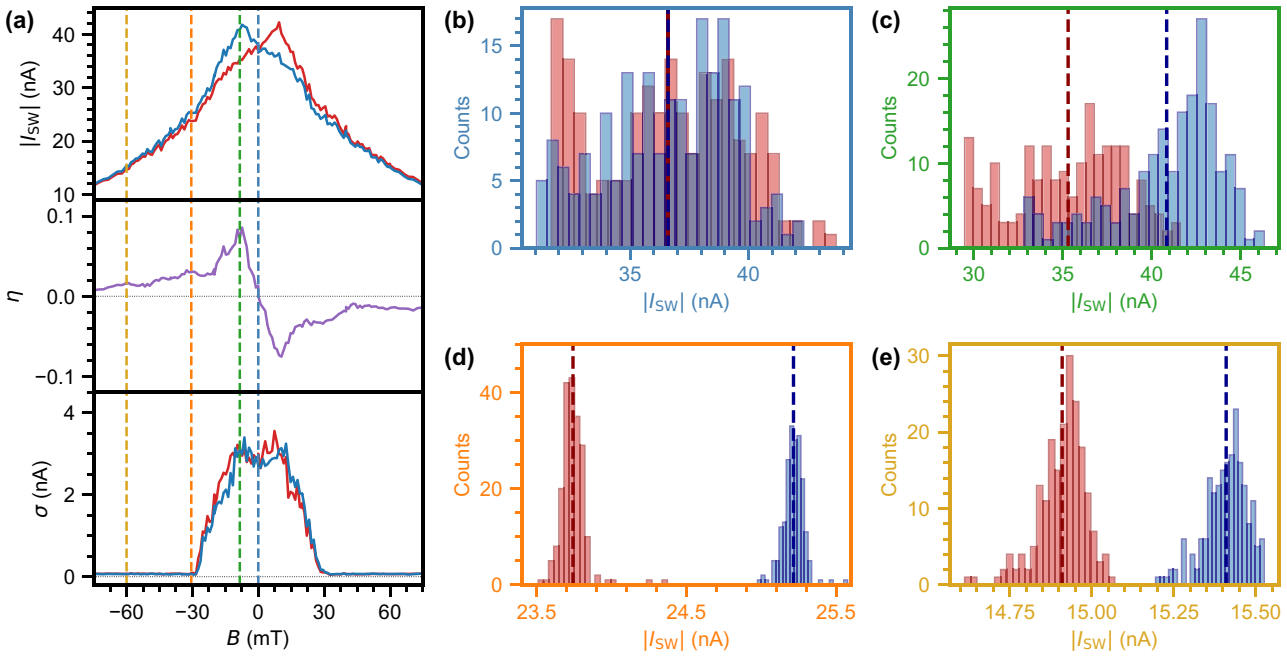

FIG. 7. Examples of switching-current distributions at various magnetic field values. (a) Top: Switching current I_{sw}^{+}, $|I_{sw}^{-}|$ as a function of magnetic field B, taken at $V_{SG} = 2.21$ V, $V_{TG} = 3.60$ V, and $\theta = 67°$ (see also Fig. 4). Middle: SDE efficiency η as a function of B. Bottom: Standard deviation σ of the switching-current distributions as a function of magnetic field. At $|B| < 30$ mT, the distributions have a larger spread. We presume this results from heating of the mixing chamber near $B = 0$ T due to the presence of magnetic components in the sample puck. (b) Switching-current distributions at $B = 0$ T. Despite the large spread of the distributions, the average switching current for both current-bias polarities is the same. (c) At $B = 10$ mT, I_{sw}^{+} and $|I_{sw}^{-}|$ differ significantly, which results in a diode efficiency η of almost 0.1. (d) At $B > 30$ mT, heating effects are diminished, which results in sharper distributions. Also displayed in Fig. 1. (e) At higher fields, the distributions remain sharp but move closer together as the SDE is diminished.

of η versus θ and either V_{SG} or V_{TG}, notably in Figs. 2, 3, 15, and 23. In each figure, the typically small offset is subtracted from the raw data. From the fits we also obtain the R^2 value, and set a threshold of $R^2 > 0.85$ for a good fit. In addition, we get the standard deviations of the three fitting parameters σ_a, σ_c, and σ_d. Analysis and raw switching-current maps of the four aforementioned figures is shown in Figs. 9, 10, 11, 16, and 24.

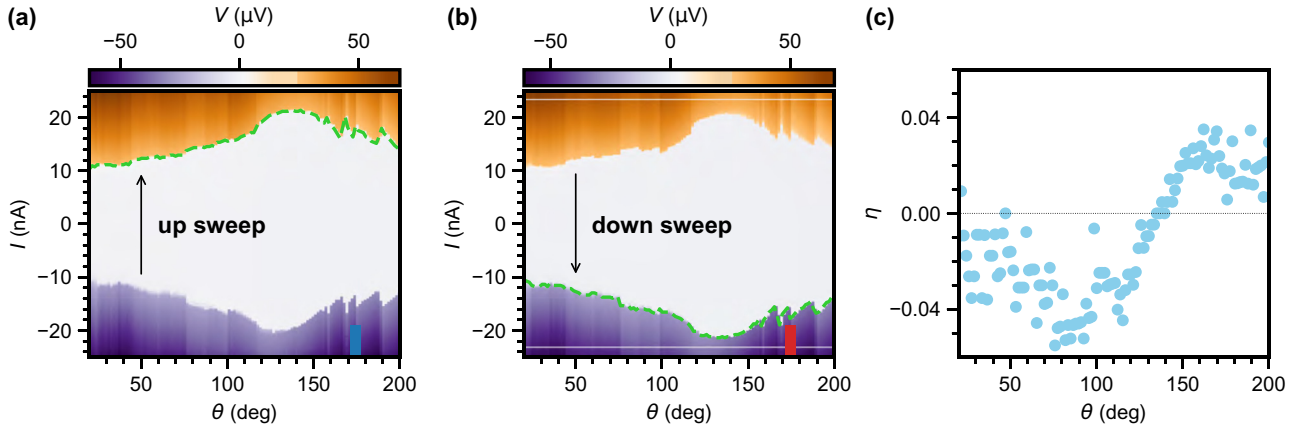

FIG. 8. SDE measured in a dc setup. (a),(b) I-V curves recorded as a function of θ at $V_{SG} = 3.0$ V, $V_{TG} = 2.0$ V, and $B = 30$ mT. The data are taken in a two-terminal geometry and are corrected for a series resistance of 5815 Ω. Dashed green lines indicate the extracted switching currents. The curves shown in Fig. 1(c) are taken from these maps at the locations indicated by the colored bars ($\theta = 174°$). (c) Diode efficiency η taken from the dc maps in (a). The dc setup takes only a single value of the switching current, such that the stochastic nature of the switching current results in a large spread in η as a function of θ. Moreover, $\eta(\theta)$ appears to be nonsinusoidal, in agreement with the high-field data shown in Figs. 4 and 13.

APPENDIX B: ADDITIONAL DATA

In Appendix B, we present complementary characterization data of the SDE in InSb/Al hybrid devices. The Figs. 19–24 systematically analyze the SDE's response to various external parameters. Analysis of cross-capacitance between tunnel gate (V_{TG}) and super gates (V_{SG}) in Fig. 19 reveals that while the SDE efficiency drops sharply below $V_{SG} = 1.15$ V, conductance maps indicate minimal cross-coupling between the gates. Figure 20 demonstrates robust SDE behavior under parallel magnetic fields, mapping diode efficiency η versus V_{SG} and B_z. The corresponding switching current maps in Fig. 21 correlate gate tuning and field alignment with SDE characteristics. Figure 22 examines rapid SDE sign inversion under high parallel Zeeman fields, showing switching current modulation across tunnel gate resonances. Device reproducibility is confirmed in Fig. 23 through angular (θ) and V_{SG} dependence measurements on a second device, consistently showing SDE suppression below $V_{SG} = 1.15$ V. In Fig. 24, we present switching current maps and our analysis of the sinusoidal fits of $\eta(\theta)$ underlying the data shown in Fig. 23.

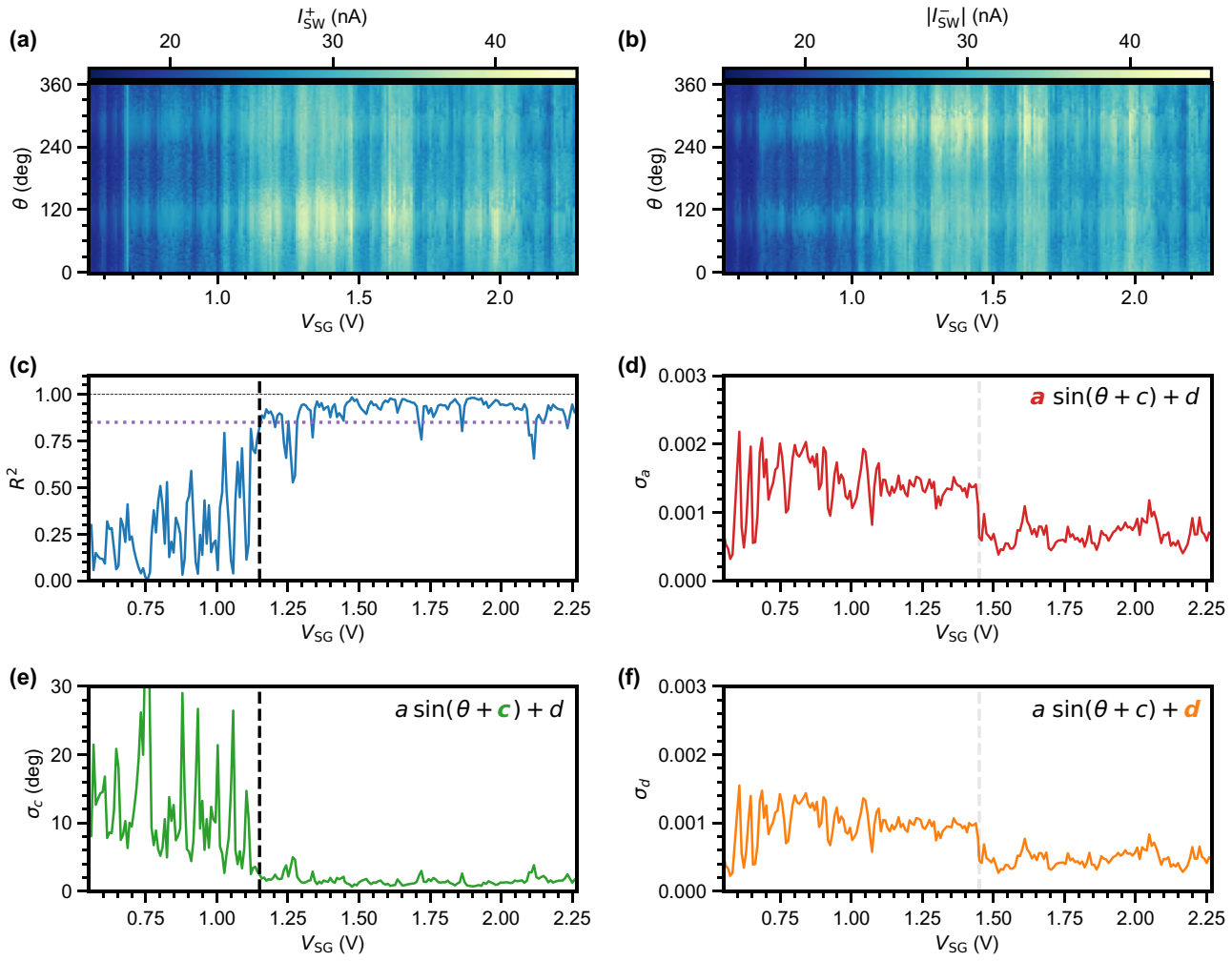

FIG. 9. Switching current and analysis underlying Fig. 2. (a),(b) I_{sw}^{+} and $|I_{sw}^{-}|$ versus V_{SG} and θ. (c) R^2 of the sinusoidal fit to the data. At $V_{SG} < 1.15$ V, R^2 quickly drops far below the threshold value of 0.85, indicating a poor sinusoidal fit. (d) Standard deviation σ_a of the amplitude of the sine fits. (e) Standard deviation σ_c of the phase of the sine fits. At $V_{SG} < 1.15$ V, the phase becomes poorly defined. (f) Standard deviation σ_d of the offset of the sine fits. In (d),(f), the dashed gray line corresponds to a change in the measurement setup where we switched from sequential detection of I_{sw}^{+} and $|I_{sw}^{-}|$ to simultaneous detection. As a result, the measurement time is halved and the thermal stability of the device increased, creating a more-accurate fit of the amplitude and offset of the sine functions.

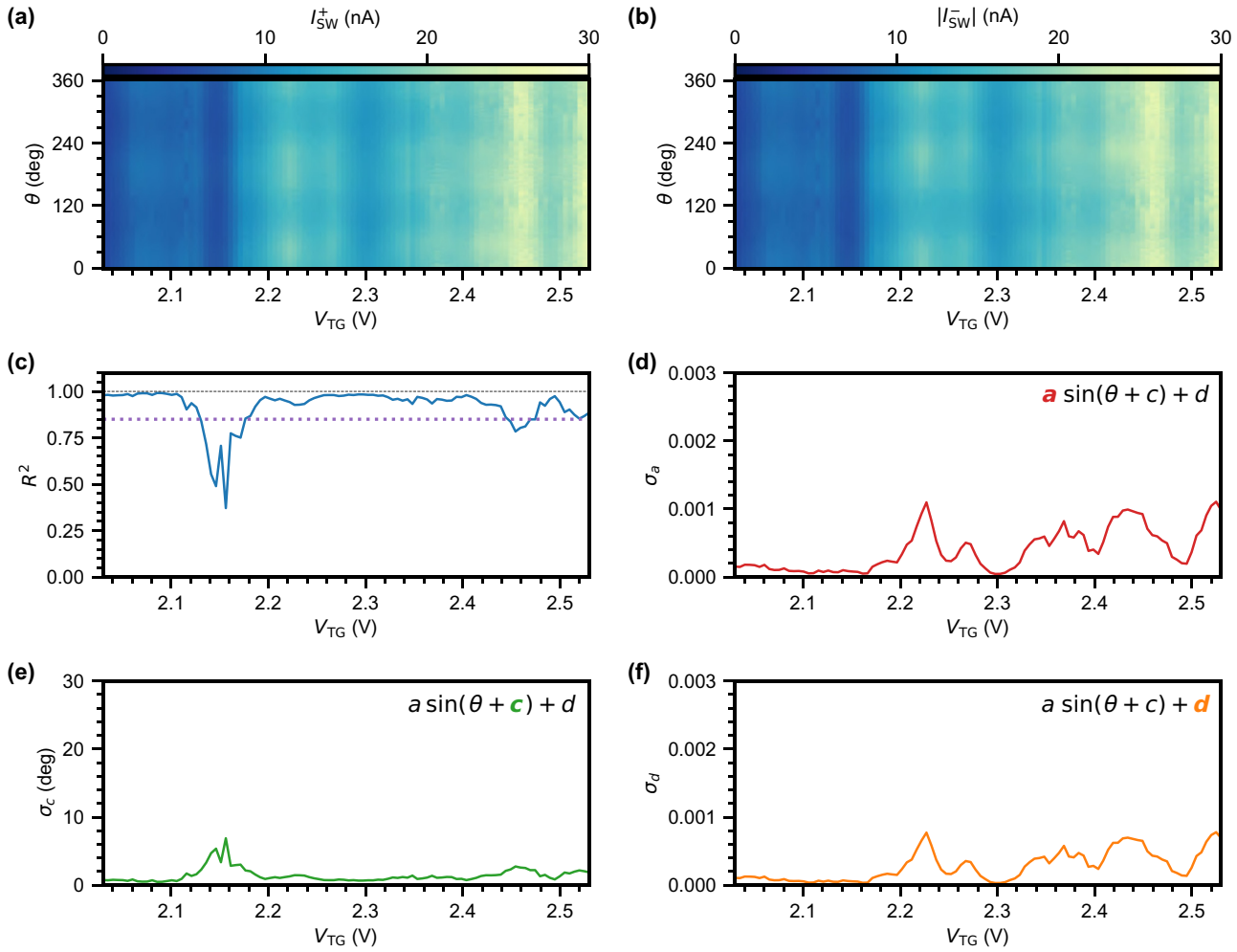

FIG. 10. Switching current and analysis underlying Figs. 3(a)–3(c) at $\mathbf{V_{SG} = 2.0}$ V. (a),(b) I^+_{sw} and $|I^-_{sw}|$ versus V_{TG} and θ. (c) R^2 of the sinusoidal fit to the data. R^2 remains above 0.85 over a large range of tunnel-gate voltages and corresponding junction transmission, indicating a good sinusoidal fit. (d) Standard deviation σ_a of the amplitude of the sine fits. (e) Standard deviation σ_c of the phase of the sine fits. (f) Standard deviation σ_d of the offset of the sine fits.

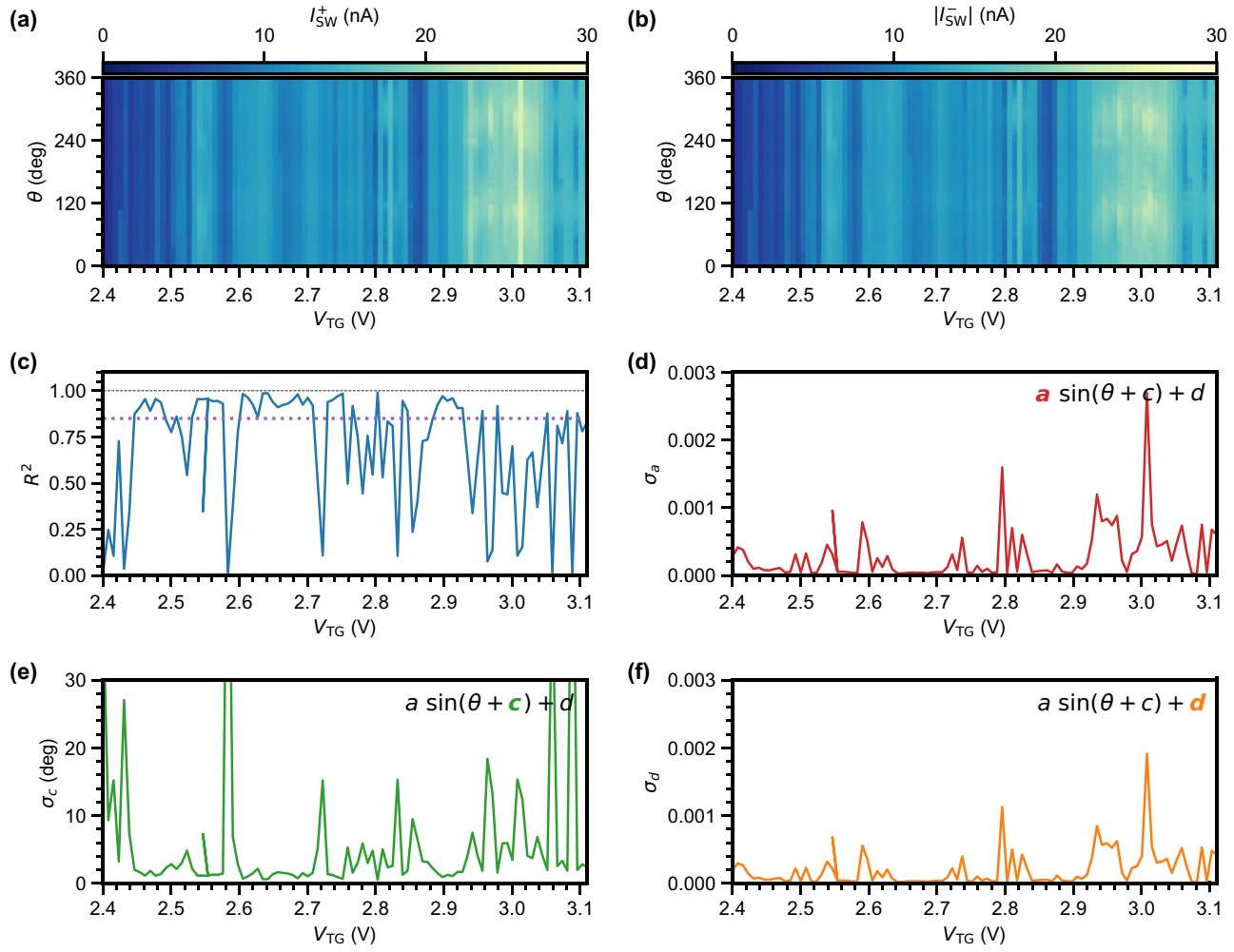

FIG. 11. Switching current and analysis underlying Figs. 3(d)–3(f) at $\mathbf{V_{SG} = 0.8}$ V. (a),(b) I_{sw}^{+} and $|I_{sw}^{-}|$ versus V_{TG} and θ. (c) R^2 of the sinusoidal fit to the data. R^2 often drops below 0.85, indicating a nonsinusoidal SDE resulting from junction physics. (d) Standard deviation σ_a of the amplitude of the sine fits. (e) Standard deviation σ_c of the phase of the sine fits. (f) Standard deviation σ_d of the offset of the sine fits.

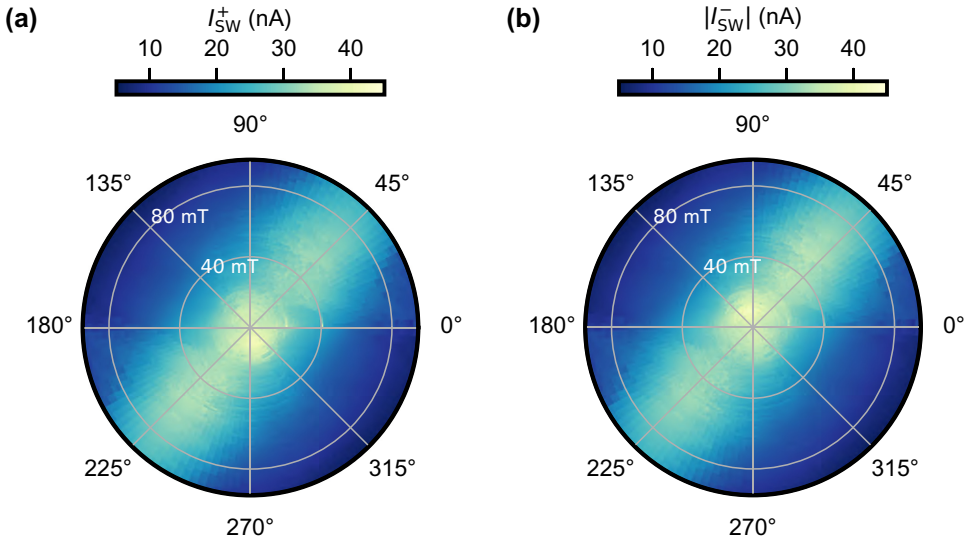

FIG. 12. Switching current and analysis underlying Fig. 4. (a) Polar plot of I_{sw}^{+}, with θ on the polar axis and B on the radial axis. (b) Polar plot of $|I_{sw}^{-}|$, with θ on the polar axis and B on the radial axis.

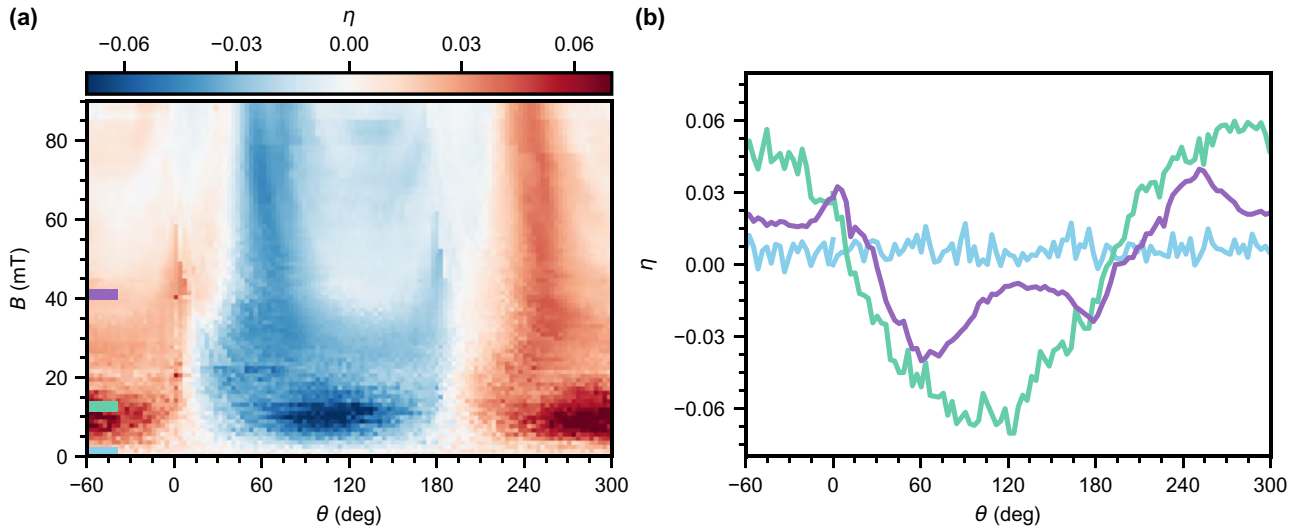

FIG. 13. Regular plot of the diode efficiency versus field magnitude; same data as in Fig. 4. (a) Regular plot of η as a function of rotating field with increasing magnitude. (b) Line cuts of η as a function of θ at various magnetic field values taken at the locations indicated by the colored bars in (a). At $B = 0$ mT (light blue), the SDE is absent. At $B = 12$ mT (light green), the SDE is sinusoidal, $\eta \propto \sin(\theta)$. At $B = 41$ mT (purple), the diode efficiency η becomes proportional to $\sin(\pi \sin(\theta))$, as predicted by Pal *et al.* [19].

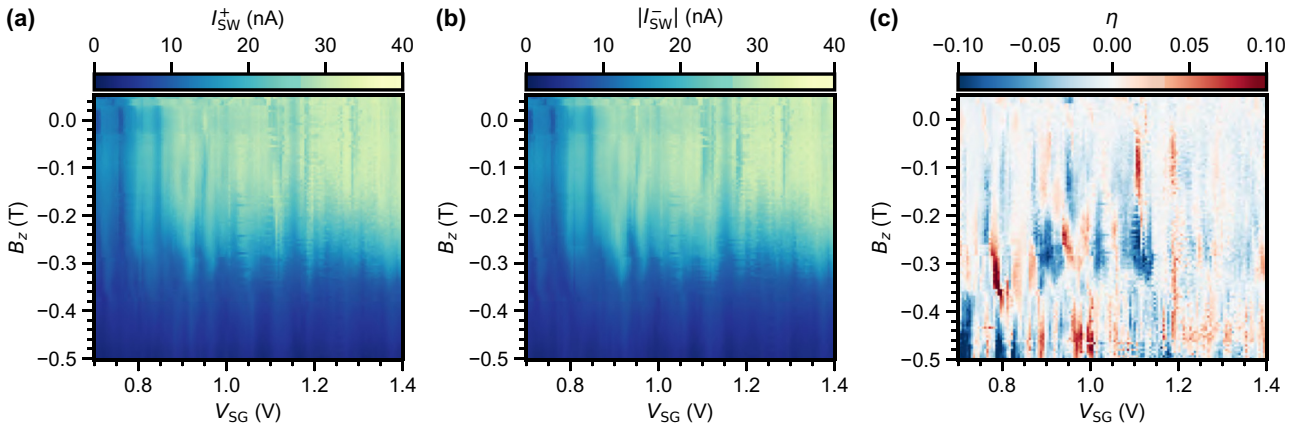

FIG. 14. Switching current and analysis underlying Fig. 5. (a),(b) I_{sw}^{+} and $|I_{sw}^{-}|$ versus V_{SG} and B_z. (c) η versus V_{SG} and B_z. Same plot as Fig. 5(a), with the difference being that Fig. 5(a) uses the absolute value of B_z presented here and is cropped at $B_z = 0$ *T*.

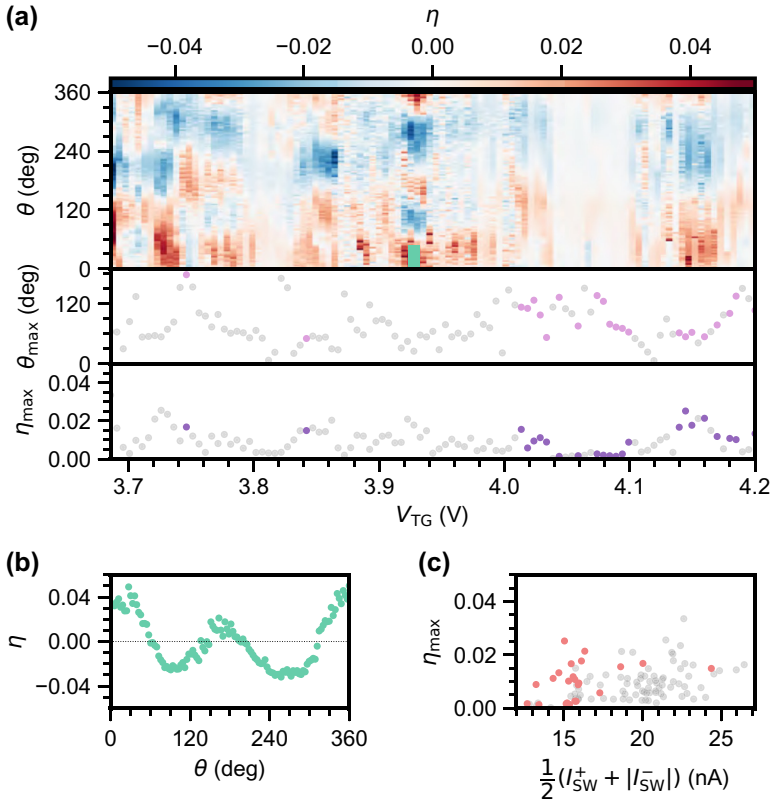

FIG. 15. SDE dependence on tunnel-gate voltage. (a) Top: Diode efficiency η versus V_{TG} and θ. Taken at a low super-gate voltage $V_{SG} = 0.7$ V and $B = 12$ mT. Middle: Estimation of the maximum-efficiency angle θ_{max}. Bottom: Maximum diode efficiency η_{max}. (b) Example of the SDE taken at the location indicated by the colored bar in (a). The diode efficiency η is proportional to $\sin(\pi \sin(\theta))$. (c) η_{max} as a function of average switching current, taken along $\theta = 105^\circ$. In all panels, gray data points correspond to a poor sinusoidal fit ($R^2 < 0.85$) of η as a function of θ.

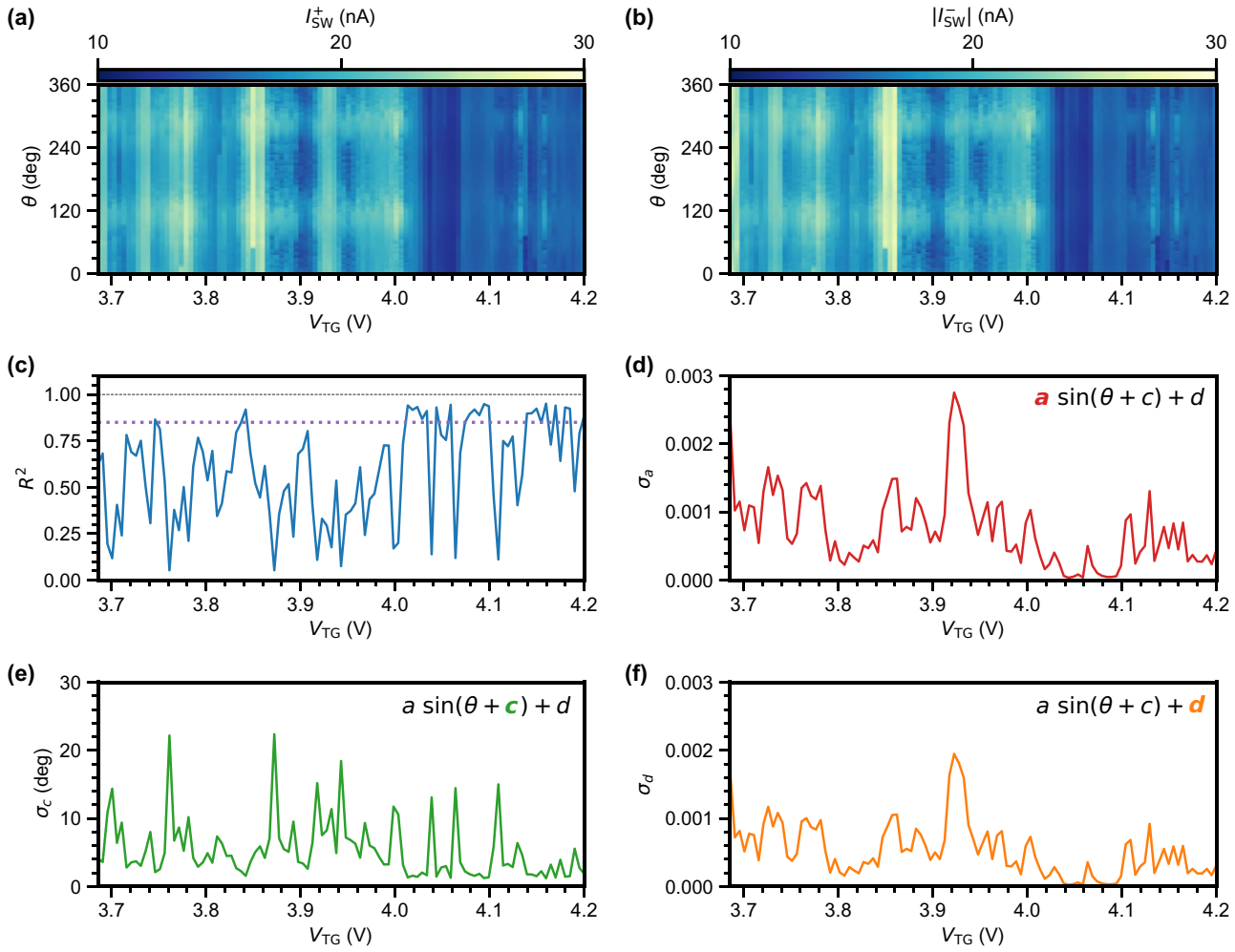

FIG. 16. Switching current and analysis underlying Fig. 15. (a),(b) I_{sw}^{+} and $|I_{sw}^{-}|$ versus V_{TG} and θ. (c) R^2 of the sinusoidal fit to the data. R^2 mostly stays below 0.85, indicating a nonsinusoidal SDE resulting from junction physics. (d) Standard deviation σ_a of the amplitude of the sine fits. (e) Standard deviation σ_c of the phase of the sine fits. (f) Standard deviation σ_d of the offset of the sine fits.

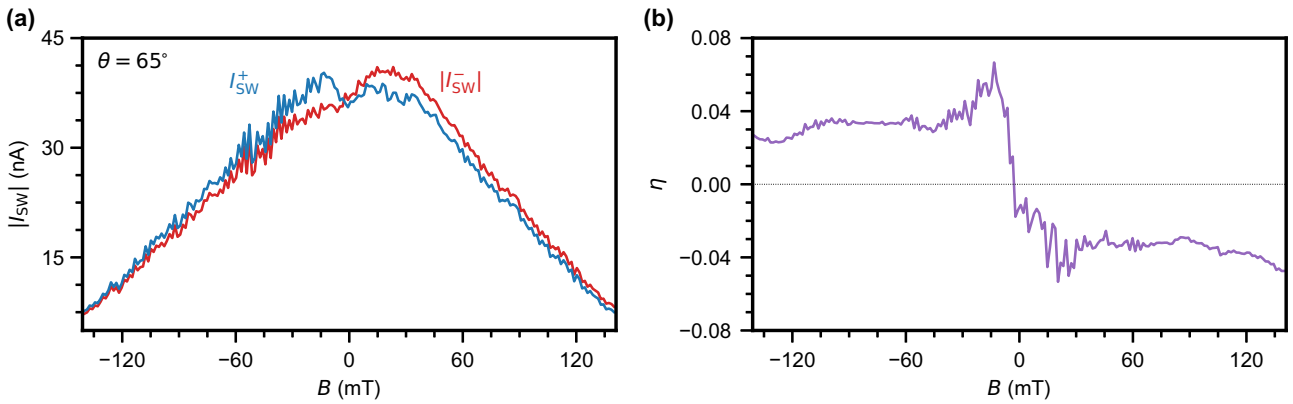

FIG. 17. Persistent SDE at a high field perpendicular to the nanowire axis. (a) I_{sw}^{+} and $|I_{sw}^{-}|$ versus B, taken at $V_{SG} = 2.21$ V, $V_{TG} = 3.61$ V, and $\theta = 65°$. (b) η versus B. The SDE persists up to a high perpendicular magnetic field $B = 140$ mT. Above this magnetic field value at this particular field angle, the Al shell on the nanowire starts to turn normal. In this case, the junction resistance below the switching current becomes finite and the I-V curve becomes smooth, so it is difficult to set the appropriate threshold for switching-current detection.

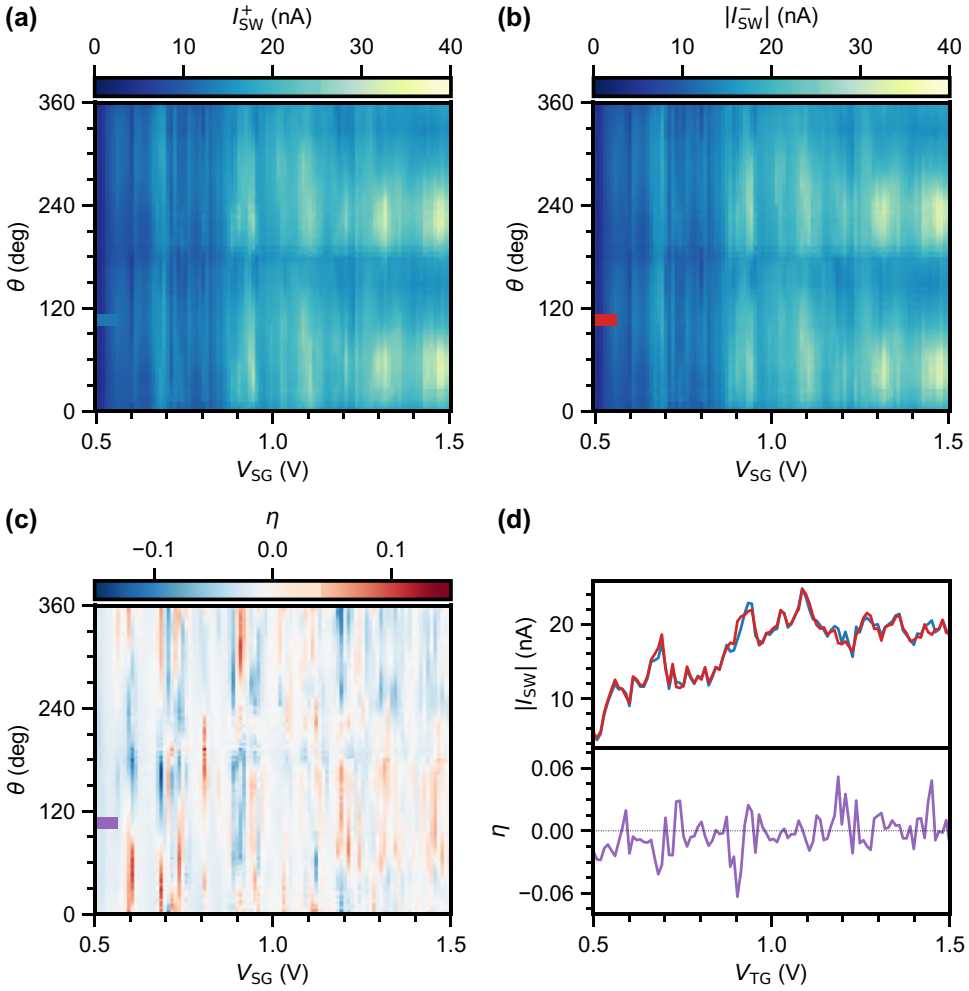

FIG. 18. SDE at a high field perpendicular to the nanowire axis. (a),(b) I^+_{sw} and $|I^-_{sw}|$ versus V_{SG} and θ, taken at $V_{TG} = 3.61$ V and $B = 60$ mT. (c) η versus V_{SG} and θ. (d) I^+_{sw}, $|I^-_{sw}|$, and η taken at the maximum-efficiency angle $\theta = 105^\circ$. The SDE frequently inverts sign as the supergate voltage is changed.

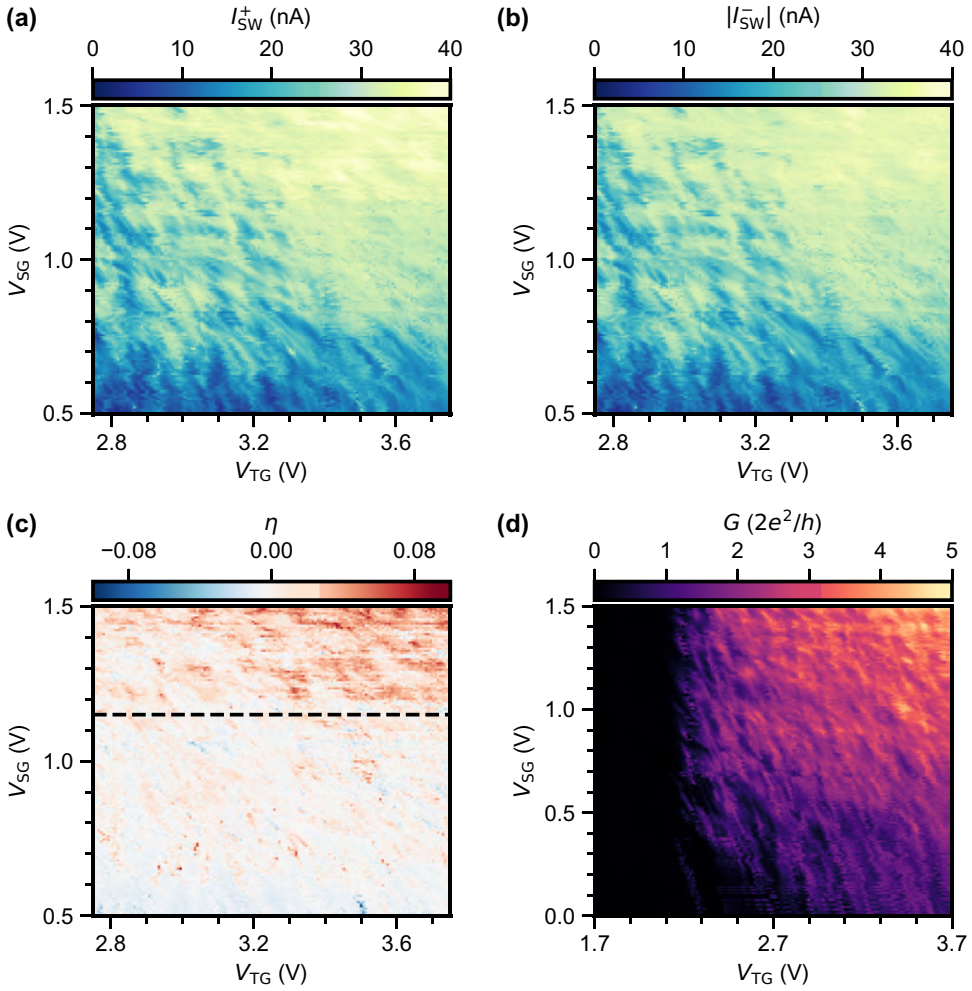

FIG. 19. Cross-capacitance between the tunnel gate and super gates. (a),(b) I_{sw}^{+} and $|I_{sw}^{-}|$ versus V_{TG} and V_{TG}, taken at $B = 12$ mT and $\theta = 105^{\circ}$. (c) η versus V_{TG} and V_{SG}. At $V_{SG} < 1.15$ V (dashed line), the SDE is strongly reduced. (d) Device conductance as a function of V_{TG} and V_{SG}, showing a minimal cross-capacitance between the gates. Data taken by application of a small bias voltage $V_{dc} = 1$ mV across the device and measurement of the resulting current I, such that $G = I/V_{dc}$.

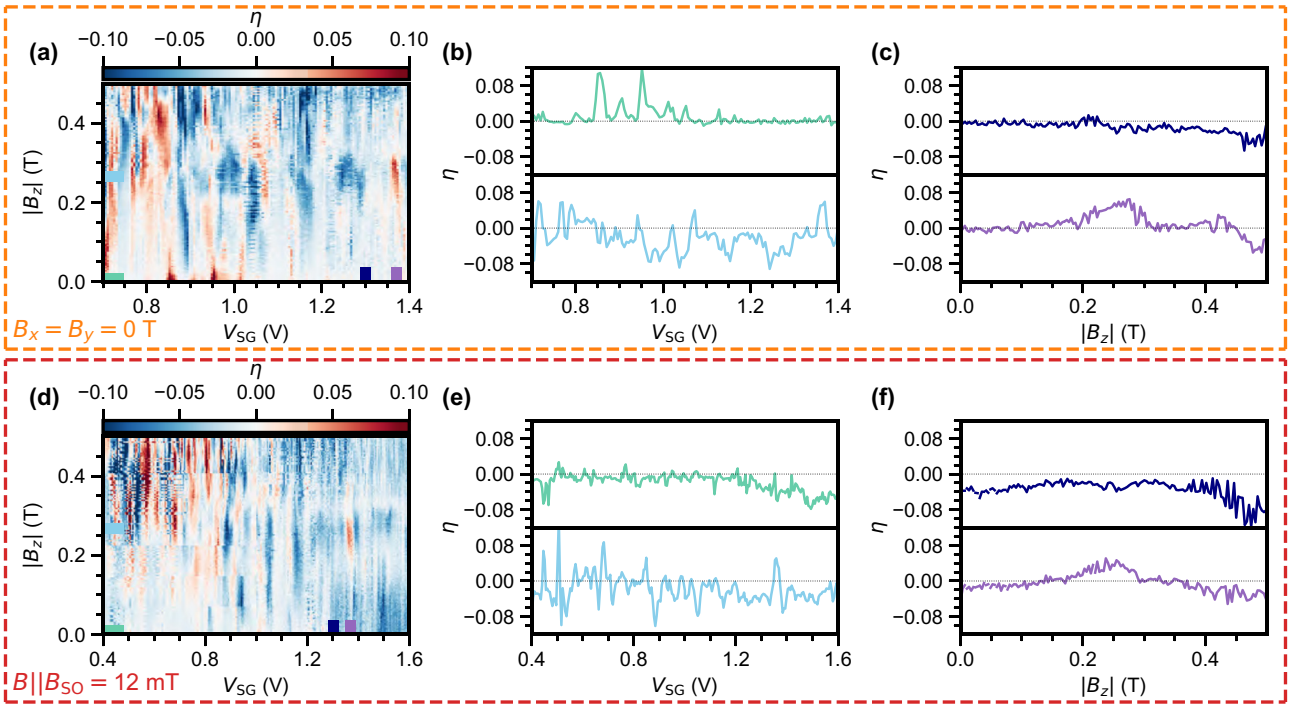

FIG. 20. Evolution of the superconducting diode effect as a function of magnetic field parallel to the nanowire axis. (a)–(c) Diode efficiency η as a function of super-gate voltage V_{SG} and parallel magnetic field B_z without any magnetic field component perpendicular to the nanowire axis. (b) Examples of η as a function of V_{SG} taken at locations indicated by the colored bars in (a). (c) Examples of η as a function of B_z taken at locations indicated by the colored bars in (a). (d),(e) Diode efficiency η as a function of super-gate voltage V_{SG} and parallel magnetic field B_z with a small field applied along the maximum-efficiency angle, $B = 12$ mT, and $\theta = 105°$. (e) Examples of η as a function of V_{SG} taken at locations indicated by the colored bars in (d). (f) Examples of η as a function of B_z taken at locations indicated by the colored bars in (d). A perpendicular component of the magnetic field does not alter the observed SDE significantly. Thus, we do not attribute the observations to subband physics as predicted by Legg *et al.* [9].

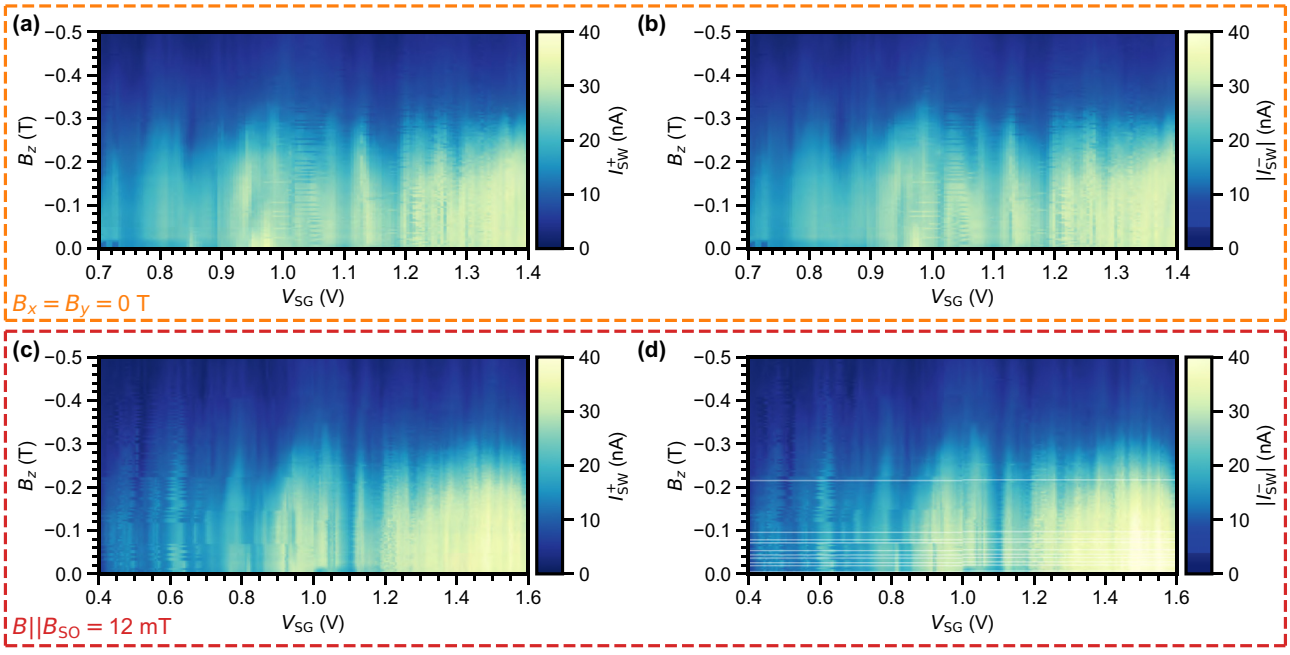

FIG. 21. Switching-current maps underlying Fig. 20. (a),(b) I_{sw}^{+} and $|I_{sw}^{-}|$ versus V_{SG} and B_z corresponding to Figs. 20(a)–20(c). (c),(d) I_{sw}^{+} and $|I_{sw}^{-}|$ versus V_{SG} and B_z corresponding to Figs. 20(d)–20(f).

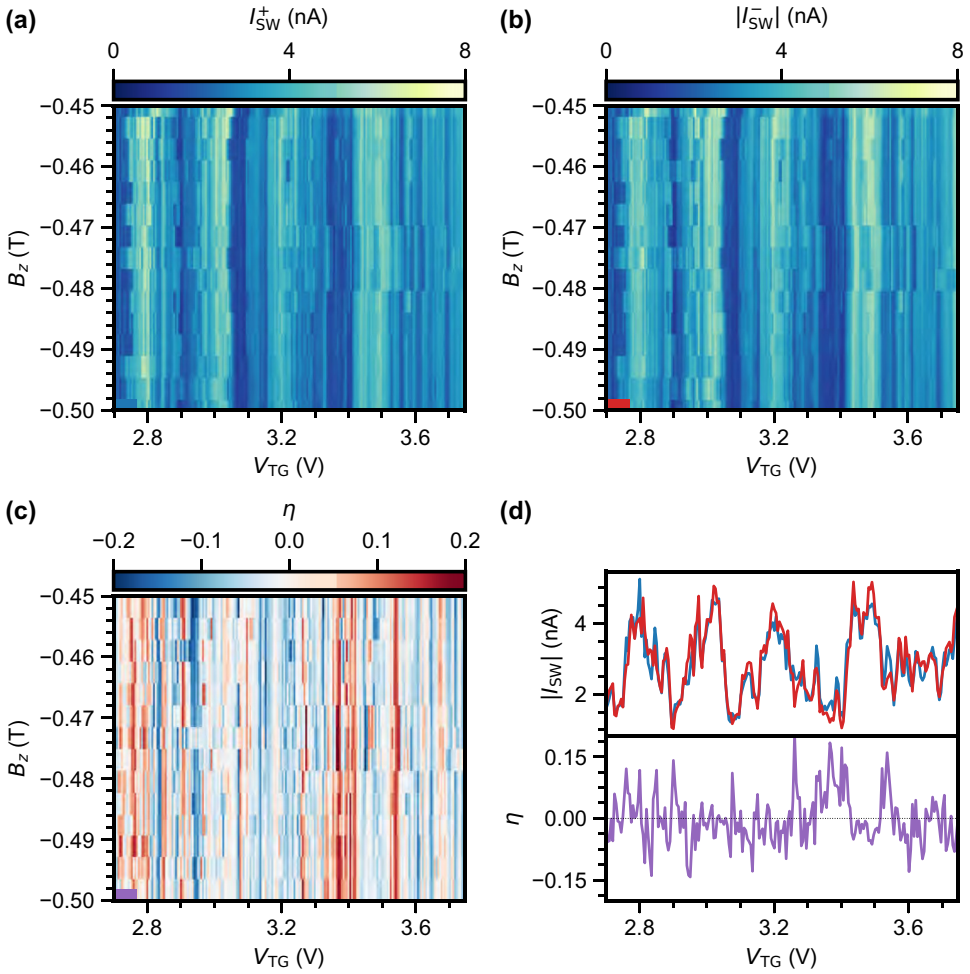

FIG. 22. Rapid sign inversion under a high parallel Zeeman field. (a),(b) I_{sw}^{+} and $|I_{sw}^{-}|$ versus V_{TG} and B_z. The tunnel-gate voltage sweeps across many resonances in the junction, causing a modulation of the switching current. Taken at $V_{SG} = 0.7$ V. (c) η versus V_{TG} and B_z. As the tunnel gate sweeps across junction resonances, the diode efficiency frequently inverts its sign and its magnitude is strongly modulated. (d) I_{sw}^{+}, $|I_{sw}^{-}|$, and η as a function of V_{TG} at $B_z = -0.5$ T.

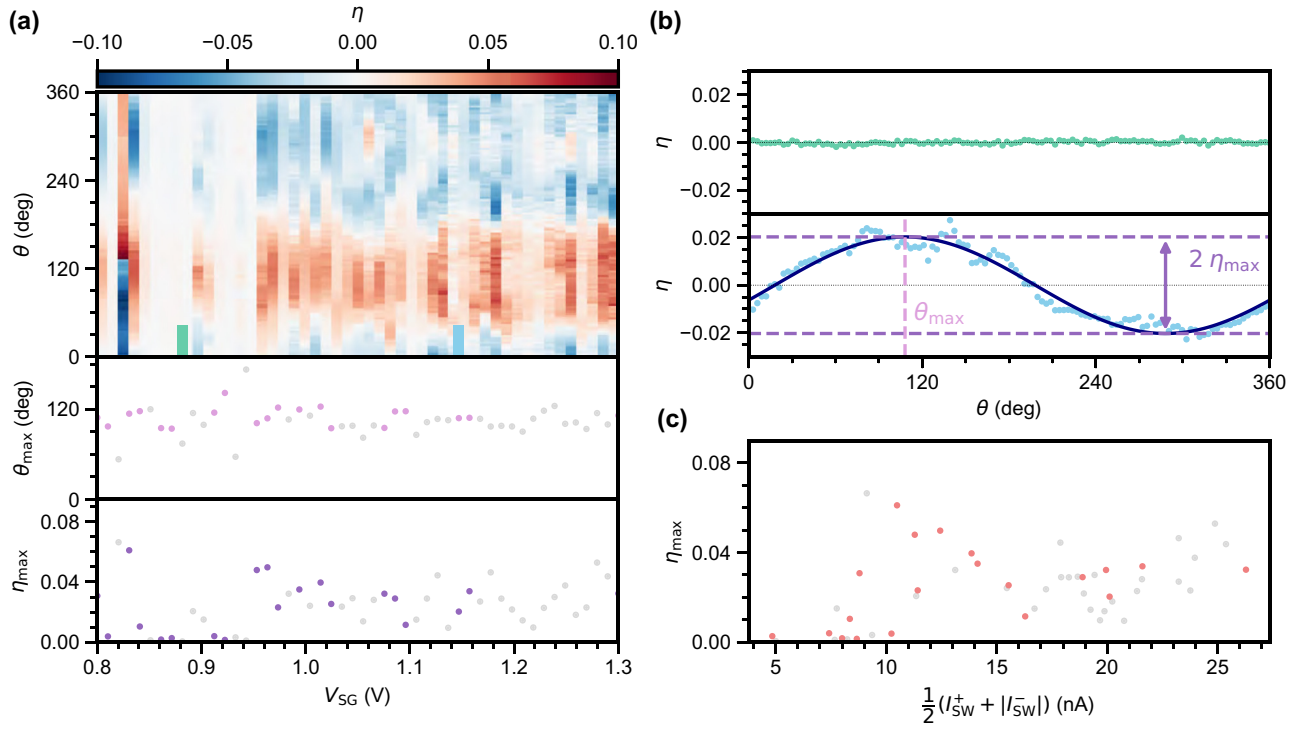

FIG. 23. Reproduction of the dependence of the superconducting diode effect on super-gate voltage on a second device. (a) Top: Diode efficiency η as a function of super-gate voltage V_{SG} and θ, taken with $V_{TG} = 4.5$ V and $B = 12$ mT. Middle: Estimation of the maximum-efficiency angle θ_{max} underneath the hybrid. Bottom: Maximum diode efficiency η_{max} as a function of V_{SG}. The dashed black line indicates that the diode effect is suppressed at $V_{SG} < 1.15$ V. (b) Top: Lack of an SDE. Bottom: Presence of an SDE. Line cuts taken from the top panel in (a) at locations indicated by the colored bars. In the bottom panel, the dashed pink line depicts the maximum-efficiency angle, whereas the maximum diode efficiency is depicted by the dashed purple lines. (c) η_{max} as a function of average switching current, taken along $\theta = 105^{\circ}$. In all panels, gray data points correspond to a poor sinusoidal fit ($R^2 < 0.85$) of η as a function of θ.

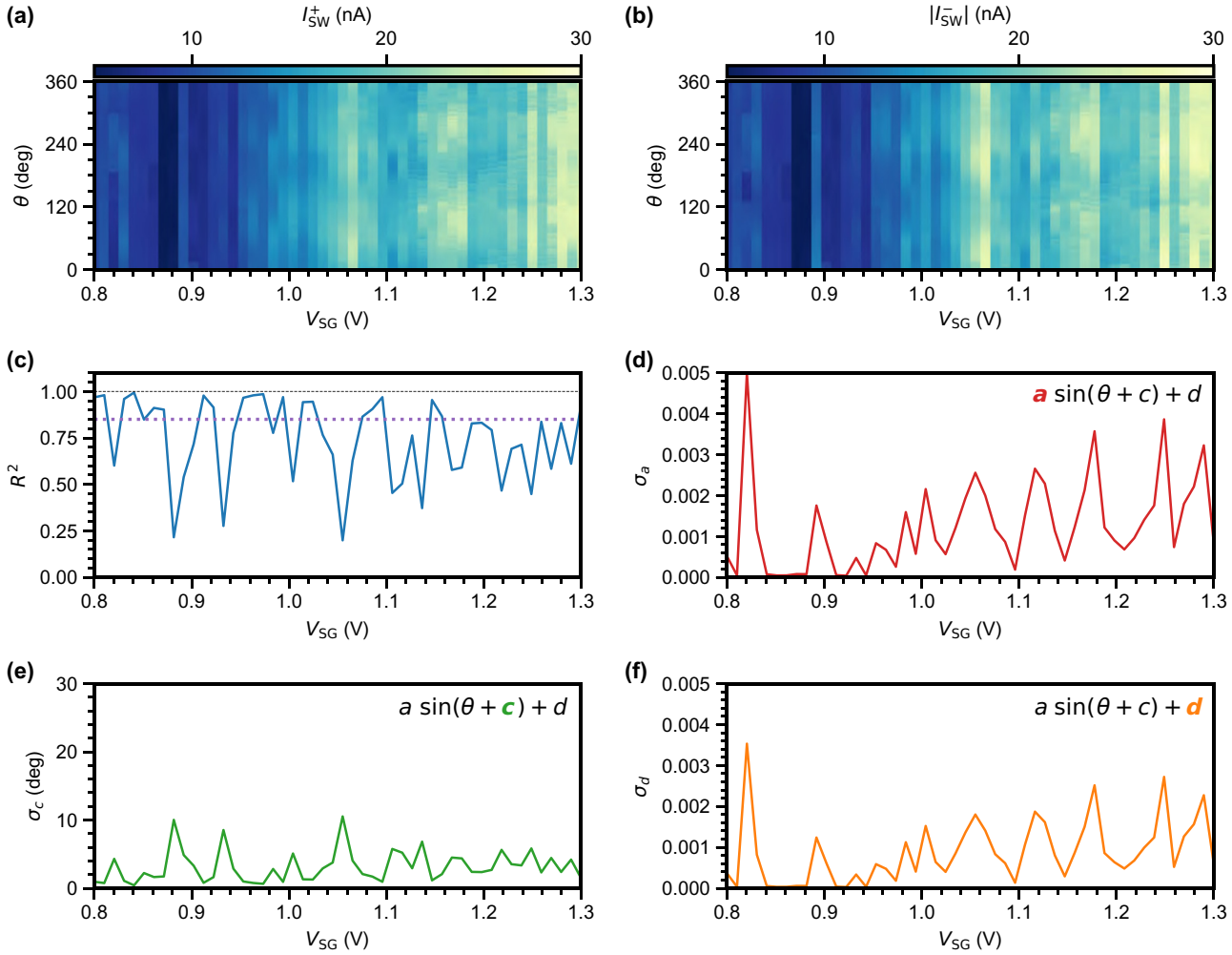

FIG. 24. Switching current and analysis underlying the reproduction device (see Fig. 23). (a),(b) I^{+}_{sw} and $|I^{-}_{sw}|$ versus V_{SG} and θ. (c) R^2 of the sinusoidal fit to the data. R^2 oscillates around 0.85, indicating an SDE due to a mix of junction and lead physics. (d) Standard deviation σ_a of the amplitude of the sine fits. (e) Standard deviation σ_c of the phase of the sine fits. (f) Standard deviation σ_d of the offset of the sine fits.

[1] F. Ando, Y. Miyasaka, T. Li, J. Ishizuka, T. Arakawa, Y. Shiota, T. Moriyama, Y. Yanase, and T. Ono, Observation of superconducting diode effect, Nature **584**, 373 (2020).

[2] V. M. Edelstein, The Ginzburg-Landau equation for superconductors of polar symmetry, J. Phys.: Condens. Matter **8**, 339 (1996).

[3] R. Wakatsuki, Y. Saito, S. Hoshino, Y. M. Itahashi, T. Ideue, M. Ezawa, Y. Iwasa, and N. Nagaosa, Nonreciprocal charge transport in noncentrosymmetric superconductors, Sci. Adv. **3**, e1602390 (2017).

[4] K. R. Jeon, J. K. Kim, J. Yoon, J. C. Jeon, H. Han, A. Cottet, T. Kontos, and S. S. Parkin, Zero-field polarity-reversible Josephson supercurrent diodes enabled by a proximity-magnetized Pt barrier, Nat. Mater. **21**, 1008 (2022).

[5] H. Isobe, S.-Y. Xu, and L. Fu, High-frequency rectification via chiral Bloch electrons, Sci. Adv. **6**, eaay2497 (2020).

[6] T. Morimoto and N. Nagaosa, Nonreciprocal current from electron interactions in noncentrosymmetric crystals: Roles of time reversal symmetry and dissipation, Sci. Rep. **8**, 1 (2018).

[7] Y. M. Itahashi, T. Ideue, S. Hoshino, C. Goto, H. Namiki, T. Sasagawa, and Y. Iwasa, Giant second harmonic transport under time-reversal symmetry in a trigonal superconductor, Nat. Commun. **13**, 1659 (2022).

[8] H. Wu, Y. Wang, Y. Xu, P. K. Sivakumar, C. Pasco, U. Filippozzi, S. S. Parkin, Y.-J. Zeng, T. McQueen, and M. N. Ali, The field-free Josephson diode in a van der Waals heterostructure, Nature **604**, 653 (2022).

[9] H. F. Legg, D. Loss, and J. Klinovaja, Superconducting diode effect due to magnetochiral anisotropy in topological

insulators and Rashba nanowires, Phys. Rev. B **106**, 104501 (2022).
[10] N. F. Yuan and L. Fu, Supercurrent diode effect and finite-momentum superconductors, Proc. Natl. Acad. Sci. **119**, e2119548119 (2022).
[11] T. Yokoyama, M. Eto, and Y. V. Nazarov, Josephson current through semiconductor nanowire with spin–orbit interaction in magnetic field, J. Phys. Soc. Jpn. **82**, 054703 (2013).
[12] T. Yokoyama, M. Eto, and Y. V. Nazarov, Anomalous Josephson effect induced by spin-orbit interaction and Zeeman effect in semiconductor nanowires, Phys. Rev. B **89**, 195407 (2014).
[13] M. Davydova, S. Prembabu, and L. Fu, Universal Josephson diode effect, Sci. Adv. **8**, eabo0309 (2022).
[14] Y. Hou, F. Nichele, H. Chi, A. Lodesani, Y. Wu, M. F. Ritter, D. Z. Haxell, M. Davydova, S. Ilić, O. Glezakou-Elbert, A. Varambally, F. S. Bergeret, A. Kamra, L. Fu, P. A. Lee, and J. S. Moodera, Ubiquitous superconducting diode effect in superconductor thin films, Phys. Rev. Lett. **131**, 027001 (2023).
[15] S. Heedt, M. Quintero-Pérez, F. Borsoi, A. Fursina, N. van Loo, G. P. Mazur, M. P. Nowak, M. Ammerlaan, K. Li, and S. Korneychuk *et al.*, Shadow-wall lithography of ballistic superconductor–semiconductor quantum devices, Nat. Commun. **12**, 1 (2021).
[16] N. van Loo, G. P. Mazur, T. Dvir, G. Wang, R. C. Dekker, J.-Y. Wang, M. Lemang, C. Sfiligoj, A. Bordin, and D. van Driel *et al.*, Electrostatic control of the proximity effect in the bulk of semiconductor-superconductor hybrids, Nat. Commun. **14**, 3325 (2023).
[17] C. Li, J. C. de Boer, B. de Ronde, S. V. Ramankutty, E. van Heumen, Y. Huang, A. de Visser, A. A. Golubov, M. S. Golden, and A. Brinkman, 4π-periodic Andreev bound states in a Dirac semimetal, Nat. Mater. **17**, 875 (2018).
[18] S. Hart, H. Ren, M. Kosowsky, G. Ben-Shach, P. Leubner, C. Brüne, H. Buhmann, L. W. Molenkamp, B. I. Halperin, and A. Yacoby, Controlled finite momentum pairing and spatially varying order parameter in proximitized HgTe quantum wells, Nat. Phys. **13**, 87 (2017).
[19] B. Pal, A. Chakraborty, P. K. Sivakumar, M. Davydova, A. K. Gopi, A. K. Pandeya, J. A. Krieger, Y. Zhang, S. Ju, and N. Yuan *et al.*, Josephson diode effect from Cooper pair momentum in a topological semimetal, Nat. Phys. **18**, 1228 (2022).
[20] J. Shabani, M. Kjaergaard, H. J. Suominen, Y. Kim, F. Nichele, K. Pakrouski, T. Stankevic, R. M. Lutchyn, P. Krogstrup, R. Feidenhans'l, S. Kraemer, C. Nayak, M. Troyer, C. M. Marcus, and C. J. Palmstrøm, Two-dimensional epitaxial superconductor-semiconductor heterostructures: A platform for topological superconducting networks, Phys. Rev. B **93**, 155402 (2016).
[21] C. Baumgartner, L. Fuchs, A. Costa, S. Reinhardt, S. Gronin, G. C. Gardner, T. Lindemann, M. J. Manfra, P. E. Faria Junior, and D. Kochan *et al.*, Supercurrent rectification and magnetochiral effects in symmetric Josephson junctions, Nat. Nanotechnol. **17**, 39 (2022).
[22] M. Gupta, G. V. Graziano, M. Pendharkar, J. T. Dong, C. P. Dempsey, C. Palmstrøm, and V. S. Pribiag, Gate-tunable superconducting diode effect in a three-terminal Josephson device, Nat. Commun. **14**, 3078 (2023).
[23] A. Sundaresh, J. I. Väyrynen, Y. Lyanda-Geller, and L. P. Rokhinson, Diamagnetic mechanism of critical current non-reciprocity in multilayered superconductors, Nat. Commun. **14**, 1628 (2023).
[24] B. Turini, S. Salimian, M. Carrega, A. Iorio, E. Strambini, F. Giazotto, V. Zannier, L. Sorba, and S. Heun, Josephson diode effect in high-mobility InSb nanoflags, Nano. Lett. **22**, 8502 (2022).
[25] B. Zhang, Z. Li, V. Aguilar, P. Zhang, M. Pendharkar, C. Dempsey, J. Lee, S. Harrington, S. Tan, and J. Meyer *et al.*, Evidence of ϕ0-Josephson junction from skewed diffraction patterns in Sn-InSb nanowires, arXiv:2212.00199.
[26] C. Leroux, A. Parra-Rodriguez, R. Shillito, A. Di Paolo, W. D. Oliver, C. M. Marcus, M. Kjaergaard, A. Gyenis, and A. Blais, Nonreciprocal devices based on voltage-tunable junctions, arXiv:2209.06194.
[27] L. J. Splitthoff, A. Bargerbos, L. Grünhaupt, M. Pita-Vidal, J. J. Wesdorp, Y. Liu, A. Kou, C. K. Andersen, and B. van Heck, Gate-tunable kinetic inductance in proximitized nanowires, Phys. Rev. Appl. **18**, 024074 (2022).
[28] A. Zwerver, T. Krähenmann, T. Watson, L. Lampert, H. C. George, R. Pillarisetty, S. Bojarski, P. Amin, S. Amitonov, and J. Boter *et al.*, Qubits made by advanced semiconductor manufacturing, Nat. Electron. **5**, 184 (2022).
[29] F. Borsoi, G. P. Mazur, N. van Loo, M. P. Nowak, L. Bourdet, K. Li, S. Korneychuk, A. Fursina, J.-Y. Wang, V. Levajac, E. Memisevic, G. Badawy, S. Gazibegovic, K. van Hoogdalem, E. P. A. M. Bakkers, L. P. Kouwenhoven, S. Heedt, and M. Quintero-Pérez, Single-shot fabrication of semiconducting–superconducting nanowire devices, Adv. Func. Mater. **31**, 2102388 (2021).
[30] V. Levajac, G. P. Mazur, N. van Loo, F. Borsoi, G. Badawy, S. Gazibegovic, E. P. Bakkers, S. Heedt, L. P. Kouwenhoven, and J.-Y. Wang, Impact of junction length on supercurrent resilience against magnetic field in InSb-Al nanowire Josephson junctions, Nano Lett. **23**, 4716 (2023).
[31] C. W. J. Beenakker and H. van Houten, Josephson current through a superconducting quantum point contact shorter than the coherence length, Phys. Rev. Lett. **66**, 3056 (1991).
[32] C. W. J. Beenakker, Universal limit of critical-current fluctuations in mesoscopic Josephson junctions, Phys. Rev. Lett. **67**, 3836 (1991).
[33] M. Zgirski, M. Foltyn, A. Savin, and K. Norowski, Flipping-coin experiment to study switching in Josephson junctions and superconducting wires, Phys. Rev. Appl. **11**, 054070 (2019).
[34] U. C. Coskun, M. Brenner, T. Hymel, V. Vakaryuk, A. Levchenko, and A. Bezryadin, Distribution of supercurrent switching in graphene under the proximity effect, Phys. Rev. Lett. **108**, 097003 (2012).
[35] D. Bouman, R. J. J. van Gulik, G. Steffensen, D. Pataki, P. Boross, P. Krogstrup, J. Nygård, J. Paaske, A. Pályi, and A. Geresdi, Triplet-blockaded Josephson supercurrent in double quantum dots, Phys. Rev. B **102**, 220505 (2020).
[36] J. D. S. Bommer, H. Zhang, O. Gül, B. Nijholt, M. Wimmer, F. N. Rybakov, J. Garaud, D. Rodic, E. Babaev, M. Troyer, D. Car, S. R. Plissard, E. P. A. M. Bakkers, K. Watanabe,

T. Taniguchi, and L. P. Kouwenhoven, Spin-orbit protection of induced superconductivity in Majorana nanowires, Phys. Rev. Lett. **122**, 187702 (2019).

[37] A. E. Antipov, A. Bargerbos, G. W. Winkler, B. Bauer, E. Rossi, and R. M. Lutchyn, Effects of gate-induced electric fields on semiconductor Majorana nanowires, Phys. Rev. X **8**, 031041 (2018).

[38] C. Reeg, D. Loss, and J. Klinovaja, Metallization of a Rashba wire by a superconducting layer in the strong-proximity regime, Phys. Rev. B **97**, 165425 (2018).

[39] P. Jarillo-Herrero, J. A. Van Dam, and L. P. Kouwenhoven, Quantum supercurrent transistors in carbon nanotubes, Nature **439**, 953 (2006).

[40] L. Han, M. Chan, D. De Jong, C. Prosko, G. Badawy, S. Gazibegovic, E. P. Bakkers, L. P. Kouwenhoven, F. K. Malinowski, and W. Pfaff, Variable and orbital-dependent spin-orbit field orientations in an InSb double quantum dot characterized via dispersive gate sensing, Phys. Rev. Appl. **19**, 014063 (2023).

[41] R. M. Lutchyn, E. P. Bakkers, L. P. Kouwenhoven, P. Krogstrup, C. M. Marcus, and Y. Oreg, Majorana zero modes in superconductor–semiconductor heterostructures, Nat. Rev. Mater. **3**, 52 (2018).

[42] E. Prada, P. San-Jose, M. W. de Moor, A. Geresdi, E. J. Lee, J. Klinovaja, D. Loss, J. Nygård, R. Aguado, and L. P. Kouwenhoven, From Andreev to Majorana bound states in hybrid superconductor–semiconductor nanowires, Nat. Rev. Phys. **2**, 575 (2020).

[43] M. W. A. de Moor, J. D. S. Bommer, D. Xu, G. W. Winkler, A. E. Antipov, A. Bargerbos, G. Wang, N. van Loo, R. L. M. O. het Veld, S. Gazibegovic, D. Car, J. A. Logan, M. Pendharkar, J. S. Lee, E. P. A. M. Bakkers, C. J. Palmstrøm, R. M. Lutchyn, L. P. Kouwenhoven, and H. Zhang, Electric field tunable superconductor-semiconductor coupling in Majorana nanowires, New J. Phys. **20**, 103049 (2018).

[44] J. Shen, G. W. Winkler, F. Borsoi, S. Heedt, V. Levajac, J.-Y. Wang, D. van Driel, D. Bouman, S. Gazibegovic, R. L. M. Op Het Veld, D. Car, J. A. Logan, M. Pendharkar, C. J. Palmstrøm, E. P. A. M. Bakkers, L. P. Kouwenhoven, and B. van Heck, Full parity phase diagram of a proximitized nanowire island, Phys. Rev. B **104**, 045422 (2021).

[45] R. S. Souto, M. Leijnse, and C. Schrade, Josephson diode effect in supercurrent interferometers, Phys. Rev. Lett. **129**, 267702 (2022).

[46] D. Szombati, S. Nadj-Perge, D. Car, S. Plissard, E. Bakkers, and L. Kouwenhoven, Josephson $\phi 0$-junction in nanowire quantum dots, Nat. Phys. **12**, 568 (2016).

[47] https://doi.org/10.5281/zenodo.7351273

[48] G. P. Mazur, N. van Loo, J.-Y. Wang, T. Dvir, G. Wang, A. Khindanov, S. Korneychuk, F. Borsoi, R. C. Dekker, and G. Badawy *et al.*, Spin-mixing enhanced proximity effect in aluminum-based superconductor–semiconductor hybrids, Adv. Mater., 2202034 (2022).

[49] https://qtwork.tudelft.nl/∼schouten/ivvi/doc-mod/docm3c.htm.